

Comprehensive analysis of the tidal effect in gravitational waves and implication for cosmology

BO WANG,^{1,2} ZHENYU ZHU,^{3,4} ANG LI,³ AND WEN ZHAO^{1,2}

¹*CAS Key Laboratory for Research in Galaxies and Cosmology, Department of Astronomy,
University of Science and Technology of China, Hefei 230026, China*

²*School of Astronomy and Space Sciences, University of Science and Technology of China, Hefei, 230026, China*

³*Department of Astronomy, Xiamen University, Xiamen 361005, China*

⁴*Institut für Theoretische Physik, Max-von-Laue-Straße 1, 60438 Frankfurt, Germany*

ABSTRACT

Detection of gravitational waves (GWs) produced by coalescence of compact binaries provides a novel way to measure the luminosity distance of GW events. Combining their redshift, they can act as standard sirens to constrain cosmological parameters. For various GW detector networks in 2nd-generation (2G), 2.5G and 3G, we comprehensively analyze the method to constrain the equation-of-state (EOS) of binary neutron-stars (BNSs) and extract their redshifts through the imprints of tidal effects in GW waveforms. We find for these events, the observations of electromagnetic counterparts in low-redshift range $z < 0.1$ are important for constraining the tidal effects. Considering 17 different EOSs of NSs or quark-stars, we find GW observations have strong capability to determine the EOS. Applying the events as standard sirens, and considering the constraints of NS's EOS derived from low-redshift observations as prior, we can constrain the dark-energy EOS parameters w_0 and w_a . In 3G era, the potential constraints are $\Delta w_0 \in (0.0006, 0.004)$ and $\Delta w_a \in (0.004, 0.02)$, which are 1-3 orders smaller than those from traditional methods, including Type Ia supernovas and baryon acoustic oscillations. The constraints are also 1 order smaller than the method of GW standard siren by fixing the redshifts through short-hard γ -ray bursts, due to more available GW events in this method. Therefore, GW standard sirens, based on the tidal effect measurement, provide a realizable and much more powerful tool in cosmology.

Keywords: gravitational waves — instrumentation: detectors — stars: neutron — cosmology: dark energy

1. INTRODUCTION

The discovery of first gravitational-wave (GW) event GW150914 (Abbott et al. 2016a,b,c,d,e,f,g), produced by the coalescence of two massive black holes (BHs), marks the new era of GW astronomy. Slightly later, the first binary neutron-star (BNS) coalescence GW event, GW170817, together with its electromagnetic (EM) counterparts, opens the window of multi-messenger GW astronomy (Abbott et al. 2017a). As the primary targets of ground-based GW detectors, such as LIGO and Virgo, the GW events of BNSs and/or NSBHs provide a new approach to explore the internal structure of NSs (Abbott et al. 2017a, 2020). In addition, these events can be treated as the standard sirens to measure various cosmological parameters (Schutz 1986), in particular the Hubble constant (Abbott et al. 2017b) and the equation-of-state (EOS) of dark energy.

The internal structure of NSs remains a challenge for current astrophysics. The ultra-high density state inside NS is an unknown field with new scientific potential. This extreme condition is inaccessible for terrestrial collider experiments and is theoretically challenging. In the EM observations of astrophysics, the constraints on EOS of NS mainly come from the measurement of radius and mass of NSs. Several NSs with a mass greater than $2M_\odot$

Corresponding author: Bo Wang
ymwangbo@ustc.edu.cn

Corresponding author: Wen Zhao
wzhao7@ustc.edu.cn

have been observed (Antoniadis et al. (2013); Fonseca et al. (2016); Arzoumanian et al. (2018); Cromartie et al. (2020); <https://stellarcollapse.org/nsmasses>), which set the maximum of allowable NS mass larger than $2M_{\odot}$ and can exclude some EOS models. However, the constraint from the mass observations is not a strong one. Lindblom proposed that the EOS of NSs can be further constrained by observing the radius-mass relation (Lindblom 1992). Related studies have been carried out and provided some constraints on the EOS (Riley et al. 2019; Miller et al. 2019). However, the uncertainties are still large in deriving constraints from current radius measurements. With the increasing sensitivities of GW detectors, and the detection of GW170817 and GW190425, the GW signal together with its EM counterpart provides a new method to explore the EOS of NSs. In the final stage of the inspiral BNS or NSBH, the tidal deformation which contains imprints of the internal structure of NS can affect the orbital motion as well as the waveform of the emitted GWs (Abdelsalhin et al. 2018; Banihashemi & Vines 2020; Bini et al. 2012; Landry 2018; Vines et al. 2011; Vines & Flanagan 2013). Thus, the EOS of NS can be determined by analyzing the GW signals from these coalescence (Read et al. 2009; Hinderer et al. 2010). GW170817 set a constraint on tidal deformability λ , whose relation with gravitational mass alone $\lambda(m)$ depends on the EOS (Love 1911; Hinderer 2008; Hinderer et al. 2010), with the observation of GW for the first time (Abbott et al. 2017a), and excluded some of the EOS models (Abbott et al. 2018a).

In order to obtain a better measurement of the EOS of NSs, it is necessary to combine the information from an ensemble of BNSs. The first idea of combining multiple sources with Fisher matrix method was reported in Ref.(Markakis et al. 2012). Del Pozzo and Agathos *et al.* proposed the first fully Bayesian study that combined information to constrain the EOS by using the tidal effects (Del Pozzo et al. 2013). Their results showed that when taking the NS mass as $1.4M_{\odot}$, tens of GW observations can constrain λ to an accuracy of $\sim 10\%$. Lackey and Wade showed that in the range of $1-2M_{\odot}$, λ can be measured to an accuracy of $10-50\%$, and the overwhelming majority of this information comes from the loudest ~ 5 GW events (Lackey & Wade 2015). In order to reduce the computational cost of the study, these authors adopted a Fisher matrix approach. Agathos *et al.* improved this analysis by including the effects of NS spin in the GW waveforms, and obtained the consistent results. Vivanco *et al.* carried out Bayesian inference and optimized the previous data processing method. They found that LIGO and Virgo are likely to place constraints on the EOS of NS similar as Ref.(Lackey & Wade 2015) by combining the first forty BNS detections (Vivanco et al. 2019).

In all these works, the authors only investigated the potential constraint of EOS of NSs by focusing on the 2G GW detectors, including LIGO (Aasi et al. 2015), Virgo (Acernese et al. 2014), KAGRA (Aso et al. 2013; Abbott et al. 2018b), and LIGO-India (Iyer et al. 2011). More importantly, these works did not consider the important role of EM counterparts in the analysis. From the observations of GW170817, it is known that BNS mergers have the EM counterparts (Abbott et al. 2017c) called “kilonova” or “macronova”, which has the nearly isotropic optical emission (Li & Paczyński 1998). For the events at low-redshift range, *i.e.* $z \lesssim 0.1$, they can be detected by various optical telescopes including Zwicky Transient Factory (ZTF), Large Synoptic Survey Telescope (LSST) (Cowperthwaite et al. 2019), Wide Field Survey Telescope (WFST) and so on. Once the EM counterparts are detected, the position and redshift of these GW events can be fixed by their host galaxies, and the degeneracy between these parameters and the EOS parameters of NS can be broken. For this reason, with the help of EM-counterpart observations for the low-redshift GW events, the constraint of NS’s EOS is expected to be significantly improved. In this article, we consider a sample of representative EOS models (Özel & Freire 2016; Zhu et al. 2018; Zhou et al. 2018; Xia et al. 2019) under the 2-solar-mass constraint. We linearly expand the relationship of NS λ - m at the average mass of NSs $1.35M_{\odot}$ as $\lambda = Bm + C$, which is similar to the treatment in Ref.(Del Pozzo et al. 2013). Based on the latest BNS merger rate (Abbott et al. 2019), we simulated a bunch of BNS sources. Using the networks of 2G, 2.5G LIGO A+ (Barsotti et al. 2018) and 3G Einstein telescope (ET) (Punturo et al. (2010), <https://www.et-gw.eu/>) and Cosmic Explorer (CE) (Abbott et al. 2017d; Dwyer et al. 2015) GW detectors, we assume that every detected GW signal at low redshift $z < 0.1$ or $z < 0.05$ has an detectable EM counterpart, which gives the precise redshift and location of the GW source. We adopt Fisher matrix approach to calculate the covariance matrix of B and C , which quantifies the capabilities of GW detectors for the determination of NS’s EOS. To highlight the importance of detectable EM counterparts, we also compare the results with those in the case without EM counterparts.

As an important issue in GW astronomy, the GW events can be treated as the standard sirens to probe the expansion history of the Universe, since the observations on the GW waveform can measure the luminosity distance d_L of the events, without having to rely on a cosmic distance ladder (Schutz 1986). For the standard sirens in low-redshift range, for instance in 2G and/or 2.5G era, one can measure the Hubble constant H_0 (Abbott et al. 2017b), and

hope to solve the H_0 -tension problem in the near future (Chen et al. 2018). While, in 3G era, a large number of high-redshift events will be detected, and the standard sirens will provide a novel way to detect the cosmic dark energy (Sathyaprakash et al. 2010; Zhao et al. 2011). The key task of this issue is to determine the redshift of these GW events. The most popular way is from the observations of their EM counterparts and/or host galaxies (Abbott et al. 2017b; Sathyaprakash & Schutz 2009; Sathyaprakash et al. 2010; Zhao et al. 2011; Cai & Yang 2017; Yan et al. 2020; Yu et al. 2020a; Tamanini et al. 2016). As mentioned above, for the low-redshift BNS mergers, the kilonovae as the primary EM counterparts could emit the nearly isotropic EM radiations (Li & Paczynski 1998), which are expected to be detected by various optical telescopes. However, for the high-redshift events, the expected EM counterparts are the short-hard γ -ray bursts (shGRBs) and the afterglows (Nakar 2007). This method of redshift measurement has three defects: First, the optical radiation of afterglow is faint, and only the nearby sources can be detected. Second, the radiation of shGRBs is believed to be emitted in a narrow cone more or less perpendicular to the plane of the inspiral. Therefore, these EM counterparts are expected to be detected only if they are nearly face-on. Third, in this method, the inclination angle ι of the events should be well determined by EM observations, which is needed to break the degeneracy between ι and d_L (Zhao & Santos 2019; Gupta et al. 2019). For these reasons, only a small fraction of the total number of BNSs are expected to be observed with shGRBs, and the application of GW sirens in cosmology is limited (Sathyaprakash et al. 2010; Zhao et al. 2011; Cai & Yang 2017; Zhao & Wen 2018).

The alternative method to measure the redshift of GW events is by counting the tidal effects in GW waveform, which was firstly proposed in (Messenger & Read 2012). The basic idea is that, the contributions of tidal effects in the GW phase evolution break a degeneracy between the mass parameters and redshift and thereby allow the simultaneous measurement of both the effective distance and the redshift for individual sources. Since this method depends only on the GW observations, all the detectable GW events can be used as standard sirens. Thus, in particular in 3G era, the number of useful events will be dramatically large. In Ref.(Del Pozzo et al. 2017), Del Pozzo *et al.* proposed for the first time to use Bayesian method to investigate the measurement errors of cosmic parameters with the GW events detected by ET. However, they directly assumed that the EOS of NS is known, did not discuss how to determine from the observations. In this article, with the EOS model determined at low redshift as a prior, in light of the tidal effect in GW, we calculate the errors of redshift Δz and luminous distance Δd_L of GW sources with the GW observation from the high-redshift range $0.1 < z < 2$ observed by the assumed 3G detector networks. Then, with the help of the property of Fisher matrix, we convert Δz and Δd_L into the errors of parameters of dark energy. For comparison, we also calculate the measurement errors of the dark energy parameters without EM counterparts observed at low redshift.

This paper is organized as follows. In Sec. 2, we review the mathematical preliminaries of GW waveforms from BNS coalescence and the response of GW detectors to these signals. In Sec. 3, we briefly introduce the EOS models adopted in this paper. In Sec. 4, we describe our method to calculate the Fisher matrix for a set of parameters required to fully describe a GW signal from BNS coalescence. In Sec. 5, we show the results of distinguishing different EOS models by 2G, 2.5G, 3G detector networks, and compare the results with and without the presence of detectable EM counterparts. In Sec. 6, we discuss the determination of the parameters for dark energy by using 3G detectors. At the end, in Sec. 7, we summarize and discuss our main results in this article.

Throughout this paper, we choose the units in which $G = c = 1$, where G is the Newtonian gravitational constant, and c is the speed of light in vacuum.

2. GW WAVEFORMS AND THE DETECTOR RESPONSE

In this section, we briefly review the detection of GWs by a ground-based network, which includes N_d GW detectors. The sizes of these detectors are all much smaller than the wavelength of GWs. We use the vector \mathbf{r}_I with $I = 1, 2, \dots, N_d$ to denote the locations of the detectors, which is given by

$$\mathbf{r}_I = R_\oplus (\sin \varphi_I \cos \alpha_I, \sin \varphi_I \sin \alpha_I, \cos \varphi_I), \quad (1)$$

in the celestial coordinate system. Here φ_I is the latitude of the detector, $\alpha_I \equiv \lambda_I + \Omega_r t$, where λ_I is the east longitude of the detector, Ω_r is the rotational angular velocity of the Earth, and R_\oplus is the radius of the Earth. In this paper, we take the zero Greenwich sidereal time at $t = 0$.

For a transverse-traceless GW signal detected by a single detector labeled by I , the response is a linear combination of the plus mode h_+ and cross modes h_\times as the following

$$d_I(t_0 + \tau_I + t) = F_I^+ h_+(t) + F_I^\times h_\times(t), \quad 0 < t < T, \quad (2)$$

Table 1. The coordinates of the interferometers used in this study. Orientation is the smallest angle made by any of the arms and the local north direction (Chu et al. 2012; Vitale & Evans 2017).

	φ	λ	γ	ζ
LIGO Livingston	30.56°	-90.77°	243°	90°
LIGO Hanford	46.45°	-119.41°	171.8°	90°
Virgo	43.63°	10.5°	116.5°	90°
KAGRA	36.25°	137.18°	0°	90°
LIGO India	19.09°	74.05°	0°	90°
Einstein Telescope in Europe	43.54°	10.42°	19.48°	60°
Cosmic Explorer in the U.S.	30.54°	-90.53°	162.15°	90°
Assumed detector in Australia	-31.51°	115.74°	0°	— —

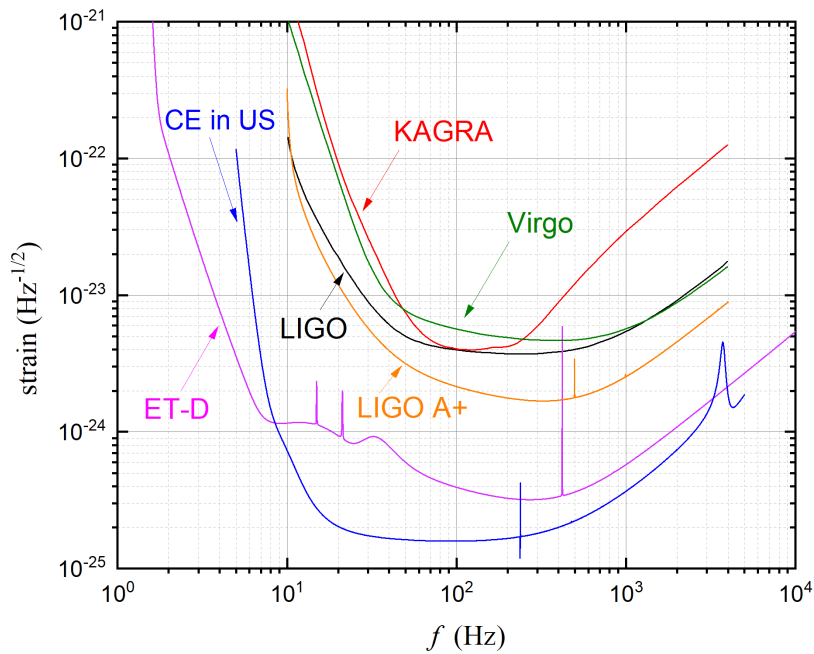


Figure 1. The design amplitude spectral density of ET-D, CE, LIGO A+, and LIGO, Virgo, KAGRA noise level (Dwyer et al. (2015); Abbott et al. (2016h, 2018b, 2017d); Barsotti et al. (2018), <https://www.et-gw.eu/>). We take the noise level of the assumed detector in Australia to be the same as CE in the U.S., and take LIGO-India to be the same as LIGO-H.

where t_0 is the arrival time of the wave at the coordinate origin and $\tau_I = \mathbf{n} \cdot \mathbf{r}_I(t)$ is the time required for the wave to travel from the origin to reach the I -th detector at time t , with $t \in [0, T]$ being the time label of the wave and T being the signal duration, and \mathbf{n} is the propagation direction of a GW. In the above, the antenna pattern functions F_I^+ and F_I^\times (Jaranowski et al. 1998; Maggiore 2008) depend on the location of the source (θ_s, ϕ_s), the polarization angle ψ_s , the latitude φ and the longitude λ of the detector on the Earth, the orientation angle γ of the detector's arms which is measured counter-clockwise from East of the Earth to the bisector of the interferometer arms, and the angle between the interferometer arms ζ . In Table 1, we list the parameters for LIGO, Virgo, KAGRA, and the LIGO-India, as well as the potential ET in Europe, CE experiment in the U.S., and the assumed detector in Australia respectively. The design amplitude spectral density for these detectors' noise (Dwyer et al. (2015); Abbott et al. (2016h, 2018b, 2017d); Barsotti et al. (2018), <https://www.et-gw.eu/>) is plotted in Fig.1. It is observed that the noises in 3G detectors are lower than the 2G detectors by about one order of magnitude, and the 2.5G detector lies in the middle. The change in orbital frequency over a single GW cycle is negligible during the inspiral phase of the binary merger. Therefore, under the stationary phase approximation (SPA) (Zhang et al. 2017a,b; Zhao & Wen 2018), the Fourier transform of

the time-series data from the I -th GW detector can be obtained as follows,

$$d_I(f) = \int_0^T d_I(t) e^{2\pi i f t} dt. \quad (3)$$

We define a whitened data set in the frequency domain in terms of the one-side noise spectral density $S_I(f)$ as the following (Wen & Chen 2010),

$$\hat{d}_I(f) \equiv S_I^{-1/2}(f) d_I(f). \quad (4)$$

For a detector network, this can be rewritten as (Wen & Chen 2010),

$$\hat{\mathbf{d}}(f) = e^{-i\Phi} \hat{\mathbf{A}} \mathbf{h}(f), \quad (5)$$

where Φ is the $N_d \times N_d$ diagonal matrix with $\Phi_{IJ} = 2\pi f \delta_{IJ} (\mathbf{n} \cdot \mathbf{r}_I(f))$, and

$$\hat{\mathbf{A}} \mathbf{h}(f) = \left[\frac{F_1^+ h_+(f) + F_1^\times h_\times(f)}{\sqrt{S_1(f)}}, \frac{F_2^+ h_+(f) + F_2^\times h_\times(f)}{\sqrt{S_2(f)}}, \dots, \frac{F_{N_d}^+ h_+(f) + F_{N_d}^\times h_\times(f)}{\sqrt{S_{N_d}(f)}} \right]^T. \quad (6)$$

Note that, F_I^+ , F_I^\times , Φ_{IJ} are all functions with respect to frequency in general, and are taken as the values at $t_f = t_c - (5/256) \mathcal{M}_c^{-5/3} (\pi f)^{-8/3}$ (Maggiore 2008) under SPA, where t_c is the binary merger time, $\mathcal{M}_c \equiv M \eta^{3/5}$ is the chirp mass of binary system with component masses m_1 and m_2 , and $M \equiv (1+z)(m_1 + m_2)$, $\eta \equiv m_1 m_2 / (m_1 + m_2)^2$. We also note that the masses in this paper are defined as the physical (intrinsic) mass, and the observed mass m_{obs} is related to the physical mass through

$$m_{\text{obs}} = (1+z)m, \quad (7)$$

where z is the redshift of the GW source.

In general, in order to estimate parameters, one needs to use the spinning inspiral-merge-ringdown merger waveform template of the compact binaries. For simplify, similar to previous works (Sathyaprakash et al. 2010; Zhao et al. 2011; Taylor & Gair 2012; Zhao & Wen 2018), we only consider the waveforms in the inspiralling stage and adopt the restricted post-Newtonian (PN) approximation of the waveform for the non-spinning systems (Sathyaprakash & Schutz 2009; Cutler et al. 1993; Blanchet & Iyer 2005), which is expected to have no significant differences in our result with the full waveforms. The SPA Fourier transform of the GW waveform from a coalescing BNS is given by (Sathyaprakash & Schutz 2009),

$$F_I^+ h_+(f) + F_I^\times h_\times(f) = \mathcal{A}_I f^{-7/6} \exp\{i[2\pi f t_c - \pi/4 + 2\psi(f/2) + \Phi_{\text{tidal}}(f)] - \varphi_{I,(2,0)}\}, \quad (8)$$

with the Fourier amplitude \mathcal{A}_I given by

$$\mathcal{A}_I = \frac{1}{d_L} \sqrt{(F_I^+(1 + \cos^2 \iota))^2 + (2F_I^\times \cos \iota)^2} \sqrt{5\pi/96} \pi^{-7/6} \mathcal{M}_c^{5/6}, \quad (9)$$

where d_L is the luminosity distance of the GW source, and ι is the inclination angle between the binary's orbital angular momentum and the line of sight. In the above, the phase ψ is contributed by the point-particle approximation of the NSs, φ is related to the detection capability of a GW detector, and Φ_{tidal} is the contribution of the finite-size deformation effects of the BNS. Under the 3.5 PN approximation for the phase, ψ and $\varphi_{I,(2,0)}$ are given by (Sathyaprakash & Schutz 2009; Blanchet & Iyer 2005)

$$\psi = -\psi_c + \frac{3}{256\eta} \sum_{i=0}^7 \psi_i (2\pi M f)^{i/3}, \quad (10)$$

$$\varphi_{I,(2,0)} = \tan^{-1} \left(-\frac{2 \cos \iota F_I^\times}{(1 + \cos^2 \iota) F_I^+} \right), \quad (11)$$

and Φ_{tidal} is given by (Messenger & Read 2012),

$$\begin{aligned} \Phi_{\text{tidal}}(f) = & \sum_{a=1}^2 \frac{3\lambda_a (1+z)^5}{128\eta M^5} \left[-\frac{24}{\chi_a} \left(1 + \frac{11\eta}{\chi_a} \right) (\pi M f)^{5/3} \right. \\ & \left. - \frac{5}{28\chi_a} (3179 - 919\chi_a - 2286\chi_a^2 + 260\chi_a^3) (\pi M f)^{7/3} \right], \end{aligned} \quad (12)$$

where the sum is over the components of the binary, $\chi_a \equiv m_a/(m_1+m_2)$, $\lambda_a \equiv \lambda(m_a)$. The parameter λ characterizes changes of the quadruple of a NS given an external gravitational field, and is comparable in magnitude with the 3PN and 3.5PN phasing terms for NSs (Messinger & Read 2012). The λ - m relation depends on the EOS models of NSs, thus different EOS models shall lead to different functions of $\lambda(m)$. Since the NS masses are approximately taken to be a Gaussian distribution with a mean of $1.35M_\odot$ and a standard deviation of $0.15M_\odot$ (Thorsett & Chakrabarty 1999; Stairs 2004; Del Pozzo et al. 2017), to parameterize EOS models, we shall express the λ - m relation as a linear function within $1\text{-}\sigma$ range of the NS mass-distribution as following

$$\lambda = B m + C, \quad (13)$$

with B and C as two tidal-effect parameters, which are expected to be determined through GW detection. Each set of values of B and C represents one EOS model of NS. EOS can be determined by fixing B and C through observations.

3. EOS MODELS AND TIDAL DEFORMABILITY

Since the astrophysical observations indicate the existence of NSs with masses larger than $\sim 2M_\odot$ (Antoniadis et al. 2013; Demorest et al. 2010; Fonseca et al. 2016; Arzoumanian et al. 2018; Cromartie et al. 2020), in this paper we consider a sample of candidate NS EOSs (Özel & Freire 2016; Zhu et al. 2018; Zhou et al. 2018; Xia et al. 2019) with varying stiffness under the 2-solar-mass constraint. The m - r relations are plotted in Fig.2 (a), and the corresponding λ - m relations are shown in Fig.2 (b). Note that we supplement 4 EOSs of quark stars, as illustrated by the dashed lines in Fig.2, which are self-bound compact stars discussed in the literature. The corresponding fitted values of B and C are listed in Table 2, together with the maximum masses and the radii of $1.35M_\odot$ stars. We mention here that ms1, ms1b are incompatible, to the 90% credibility interval, with the tidal deformability constraint from GW170817 (Abbott et al. 2017a), while H4 is marginally consistent. Among neutron star EOS models, ap4, ms1, ms1b, wff2 are outside the boundaries, to the 68.3% credibility interval, of the mass and radius constraints obtained for PSR J0030+0451 (Miller et al. 2019; Riley et al. 2019). We make the reasonable assumption that all neutron stars are described by the

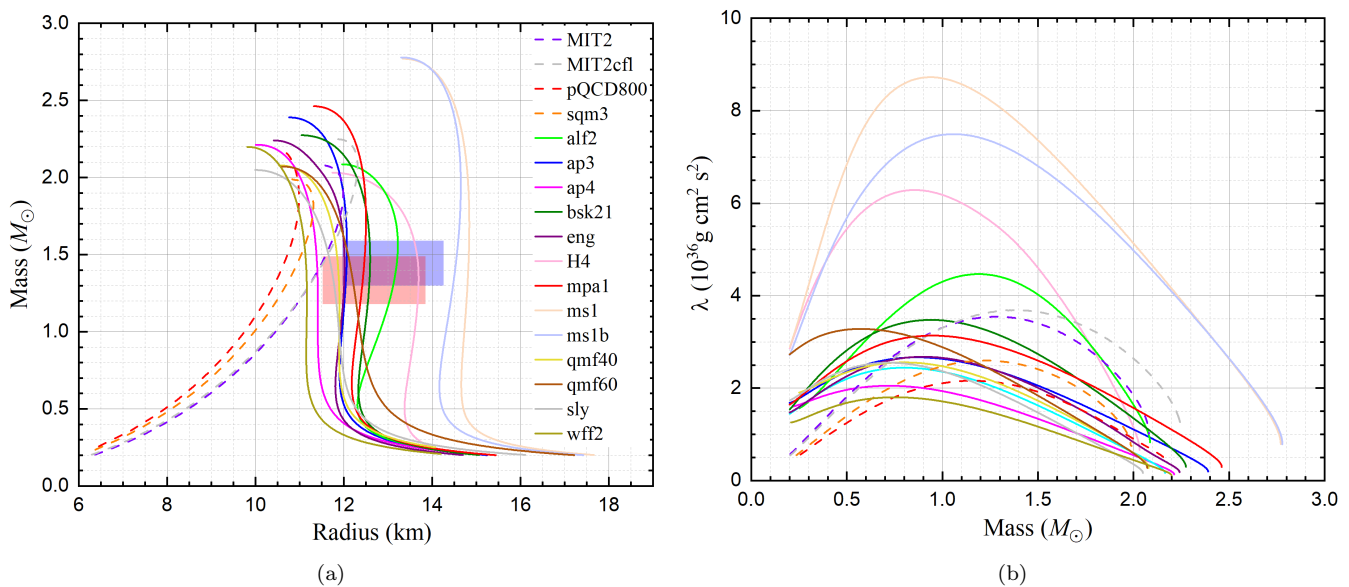


Figure 2. (a) m - r relations for various EOS models. The blue and red boxes are the m - r error ranges to the 68.3% credibility interval of the millisecond pulsar PSR J0030+0451 inferred by Ref.(Miller et al. 2019) and Ref.(Riley et al. 2019) using the NICER data, respectively. (b) λ - m relations for the EOS models, which are selected under $m_{\max} > 2M_\odot$. The maximum mass of each curve is the maximum mass for the corresponding EOS. The dashed lines are theoretical EOSs for quark stars.

same EOS (Forbes et al. 2019), *i.e.*, all NSs have the same values of B and C . By the numerical simulation of GW from BNSs with observable electromagnetic counterparts at low redshift, we shall study the discrimination of these models by networks of GW detectors .

For most BNS mergers at high redshift, the electromagnetic counterparts are not expected to be observed. However, it is found from (12) that when considering the tidal effects, z and m do not bound with each other, in contrary to the point-particle approximation (10). This property enables us to estimate redshifts by only using information coming only from the GW observations without electromagnetic counterparts, which shall be discussed in latter sections when determining the parameters of dark energy.

Table 2. The values of B and C fitted according to Eq.(13) for the EOS models in Fig.2. For each EOS, the maximum allowable mass and the radius for a NS with $1.35M_\odot$ are also listed.

EOS	$B(10^{36}\text{g cm}^2\text{s}^2/M_\odot)$	$C(10^{36}\text{g cm}^2\text{s}^2)$	$M_{\text{max}}(M_\odot)$	$R_{1.35}(\text{km})$
alf2	-1.47	6.30	2.09	13.15
ap3	-1.40	4.17	2.39	12.05
ap4	-1.34	3.36	2.21	11.40
bsk21	-1.87	5.56	2.27	12.58
eng	-1.60	4.43	2.24	12.01
H4	-3.85	10.44	2.03	13.69
mpa1	-1.37	4.67	2.46	12.43
ms1	-3.35	12.41	2.77	14.81
ms1b	-2.03	9.89	2.78	14.49
qmf40	-1.74	4.35	2.08	11.88
qmf60	-2.25	5.22	2.07	12.19
sly	-1.99	4.46	2.05	11.75
wff2	-1.24	3.04	2.20	11.16
MIT2*	-0.44	4.10	2.08	11.32
MIT2cfl*	0.14	3.47	2.25	11.33
pQCD800*	-0.77	3.10	2.17	10.50
sqm3*	-0.60	3.35	1.99	10.78

* These are the EOS models of quark stars.

4. FISHER MATRIX AND ANALYSIS METHOD

The match-filter method is commonly used to estimate the parameters from detected waveforms against certain theoretical templates. For an unbiased estimation (the ensemble average of which is the true value), according to the Cramer-Rao bound (Cramér 1946), the lower bound for the covariance matrix of estimated parameters is the inverse of the Fisher matrix (Kay 1993) when considering statistical errors, which is method-independent. Thus, the errors of the estimated parameters p_i can be calculated by using Fisher matrix F_{ij} through the expression $\langle \delta p_j \delta p_k \rangle = (F^{-1})_{jk}$ in many fields (Martinez et al. 2009). The Fisher matrix of a network including N_d independent GW detectors is given by (Finn 1992; Finn & Chernoff 1993),

$$F_{ij} = \langle \partial_i \hat{\mathbf{d}} | \partial_j \hat{\mathbf{d}} \rangle, \quad (14)$$

where $\partial_i \hat{\mathbf{d}} \equiv \partial \hat{\mathbf{d}}(f) / \partial p_i$, and $\langle a | b \rangle \equiv 2 \int_{f_{\text{low}}}^{f_{\text{up}}} \{a(f)b^*(f) + a^*(f)b(f)\} df$. For a given BNS system, $\hat{\mathbf{d}}(f)$ in Eq.(5) depends on twelve system parameters ($\mathcal{M}_c, \eta, t_c, \psi_c, \iota, \theta_s, \phi_s, \psi_s, d_L, z, B, C$), where ψ_c is defined in Eq.(10), B and C are defined in Eq.(12), and the other parameters are all defined previously. By taking the noise in detectors as stationary and Gaussian, the optimal squared signal-to-noise ratio (SNR) is given by (Finn 1992; Finn & Chernoff 1993)

$$\rho^2 = \langle \hat{\mathbf{d}} | \hat{\mathbf{d}} \rangle. \quad (15)$$

Once the total Fisher matrix F_{ij} is calculated, an estimate of the root mean square (RMS) error, Δp_i , in measuring the parameter p_i can then be calculated,

$$\Delta p_i = (F^{-1})_{ii}^{1/2}. \quad (16)$$

The correlation coefficient between two parameters will be $r_{ij} \equiv (F^{-1})_{ij}/[(F^{-1})_{ii}(F^{-1})_{jj}]^{1/2}$, Note that $r_{ij} = 0$ indicates the independency of p_i and p_j , and $|r_{ij}| = 1$ indicates the complete correlation of p_i and p_j , i.e., p_i and p_j are degenerate in data analysis, and the Fisher matrix is not invertible.

For practical computation, the analytical expression of the solution for $\partial\hat{\mathbf{d}}(f)/\partial p_i$ is usually not available, and one needs to use numerical methods. We adopt an approximation $\partial\hat{\mathbf{d}}(f)/\partial p_i \simeq (\hat{\mathbf{d}}(f; p_i + \delta p_i) - \hat{\mathbf{d}}(f; p_i))/\delta p_i$ which was used by Ref.(Zhao & Wen 2018), and calculate the Fisher matrix numerically. Note that the Fisher matrix yields only the lower limit of the covariance matrix, which might be slightly different from the corresponding results derived from Monte Carlo simulations.

5. DETERMINATION OF EOS OF THE NEUTRON STARS

To extract EOS information from the GW detection, great detector sensitivity is required. In this paper, we investigate four types of detector networks, including 2G, 2.5G and 3G detectors, for GW detection, and compare their abilities for the EOS determination.

- **LHV** one LIGO-Livingston detector, one LIGO-Hanford detector, and one Virgo detector.
- **LHVIK** LHV and additionally one LIGO-India detector and one KAGRA.
- **3LA+** Three assumed LIGO A+ detectors locate in the sites of LHV respectively.
- **ET2CE** One ET-D detector in Europe and two CE detectors in the U.S. and in Australia respectively. The optimal site localizations for this kind of network with planning 3G detectors have been studied in Ref.(Raffai et al. 2013).

The coordinates, orientations, and open angles of the detectors are listed in Table 1, the design amplitude spectral densities of the detectors' noise are shown in Fig.1. According to the detection rates in Refs.(Abbott et al. 2020, 2019), we shall generate the random BNS samples simulatively with $m_1 = m_2 = 1.35M_\odot$ at low redshift $z < 0.1$ to investigate the resolution of B and C for the tidal effects in Eq.(13).

5.1. The LHV network

We consider the case with LHV network to determine the EOS model in low redshift $z < 0.1$. Given a merger rate as $250\text{--}2810 \text{ Gpc}^{-3} \text{ y}^{-1}$ at 90% confidence level (CL) (Abbott et al. 2019), and assuming that BNSs are uniformly distributed in comoving volume, there will be $2.5 \times 10^2 \sim 2.8 \times 10^3$ BNS merger events for three-year observation. In this paper, $\text{SNR} > 10$ is taken as the criterion for detectable GW. As an illustration, we perform a numerical simulation to generate GW samples from BNS merger. In Fig. 3, the SNR distribution of the generated samples is presented. It is observed that there are 30 detectable samples among the total 250 merger events, and 384 detectable samples among the total 2800 merger events. For every detectable GW, we assume that the corresponding electromagnetic counterparts are observable at this low-redshift region, which provides the precise redshift z and location (θ_s, ϕ_s) of the source. The remaining 9 parameters ($\mathcal{M}_c, \eta, t_c, \psi_c, \iota, \psi_s, d_L, B, C$) need to be determined by GW observation. To explore the detection uncertainties of B and C , one needs to marginalize the remaining 7 parameters, which is complicated through a Bayesian approach (Del Pozzo et al. 2017). We adopt an easy-to-handle process by using Fisher matrix (Coe 2009; Amendola & Sellentin 2016). For a detectable GW sample k , we calculate the 9-parameter Fisher matrix and inverse it to get the 9-parameter covariance matrix. The removal of the rows and columns of the 7 parameters except B and C is equivalent to the marginalization of these 7 parameters, and inverting the remaining 2×2 submatrix yields the Fisher matrix $(F_{ij})_k$ of B and C . The total Fisher matrix is obtained by summing the Fisher matrixes of (B, C) over all detectable GW samples, $F_{ij} = \sum_k (F_{ij})_k$. Then, it is straightforward to get the covariance matrix of B and C as the inverse of F_{ij} , with which we can plot the error ellipse of B and C as illustrated in Fig.4 at $2\text{-}\sigma$ CL. If two error ellipses overlap, the two corresponding models of EOS cannot be distinguished from each other. We find that when taking 250 samples of merger events, under $2\text{-}\sigma$ CL, some models can be distinguished from the others, such as ms1, H4, ms1b, alf2, bsk21, qmf60, MIT2, MIT2cfl. The remaining models cannot be distinguished due to the low sensitivity of LHV. When sampling 2800 merger events, all models can be distinguished from each other.

In the above, we only consider the BNS coalescences with the same individual NS masses as $1.35M_\odot$. In reality, the actual individual masses are more likely to be different. In order to investigate the effect of different NS masses on constraining the EOS parameters, we set all the merging BNS masses as the medium numbers of the NS masses derived from GW190425, which is $m_1 = 1.75M_\odot$ and $m_2 = 1.57M_\odot$ (Abbott et al. 2020), and repeat the same simulation process as before. We find that the error ellipses of B and C are similar as in Fig.4, which leads to the same conclusion for distinguishing EOS models. So different NS masses does not significantly affect the results. However, since the

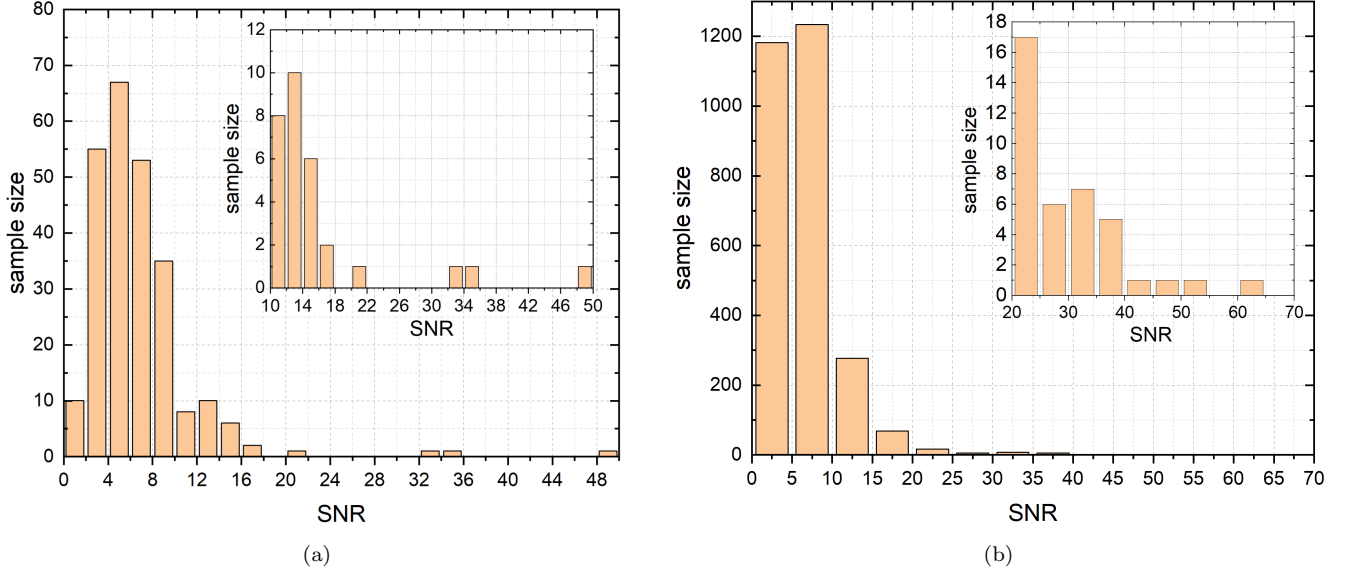


Figure 3. The SNR distribution of the samples generated in the redshift range of $z < 0.1$ detected by LHV. According to the lowest and highest event rates given in Ref.(Abbott et al. 2019), we generate a total of 250 samples in (a) and a total of 2800 samples in (b). With the threshold of $\text{SNR} > 10$, there are 30 detectable samples as shown in (a); and there are 384 detectable samples in (b).

premised λ - m relation in (13) is only valid within $1\text{-}\sigma$ range of the NS mass-distribution adopted in this paper, the differentiation of EOS models may be modified according to the true merging NS mass-distribution, which currently remains unknown unfortunately.

5.2. The LHVIK network

Next, we consider the LHVIK network. The SNR distribution is shown in Fig.5. It can be seen that when a total of 250 samples are taken, there are 66 detectable samples, more than that in LHV case. The corresponding error ellipses of B and C for different EOS models are shown in Fig.6 (a) under $2\text{-}\sigma$ CL. Compared with Fig.4 (a) by LHV, LHVIK can distinguish 5 additional EOS models, namely, sly, mpa1, ap3, pQCD800 and sqm3. When a total of 2800 samples are taken, there are 748 detectable samples, and the error ellipses are presented in Fig.6 (b). We find that all the EOS models are distinguishable. It can be seen that the error ellipses by LHVIK are slightly smaller than that by LHV. This is because the SNR by LHVIK is greater than by LHV and the number of detectable samples by LHVIK is also larger.

5.3. The 3LA+ network

Similar to the previous process, Fig.7 plots the SNR distribution by 3LA+ in the redshift range of $z < 0.1$. Among a total of 250 samples, 152 samples are detectable, and the $2\text{-}\sigma$ error ellipses of B and C are plotted in Fig.8 (a). Among a total of 2800 samples, 603 samples can be detected, and the $6\text{-}\sigma$ error ellipses are plotted in Fig.8 (b). From the two figures, it is found that all the EOS models can be distinguished by 3LA+ given any merger rate. Thus, the detection capability of 3LA+ is stronger than both LHV and LHVIK, and the proportion of samples that can be detected by 3LA+ is higher.

5.4. The ET2CE network

Similarly, the SNR distribution by the ET2CE network is plotted in Fig.9 in the redshift $z < 0.1$. Under criterion $\text{SNR} > 10$, all GW samples are detectable in the given merger rates. When the merge events are taken as the lower limit of 250, the $25\text{-}\sigma$ error ellipses of B and C are plotted in Fig.10 (a). When the merger events is taken to be its upper limit as 2800 samples, the $80\text{-}\sigma$ error ellipses are in Fig.10 (b). It is observed that all the EOS models can be distinguished for every possible merger rate. This improvement is due to the great sensitivity of the ET2CE network.

In order to compare the detection capabilities of different detector networks, at $z < 0.1$ with a total of 250 samples, we take the average of the $2\text{-}\sigma$ errors of B and C given by each network over all the EOS models. The result is shown

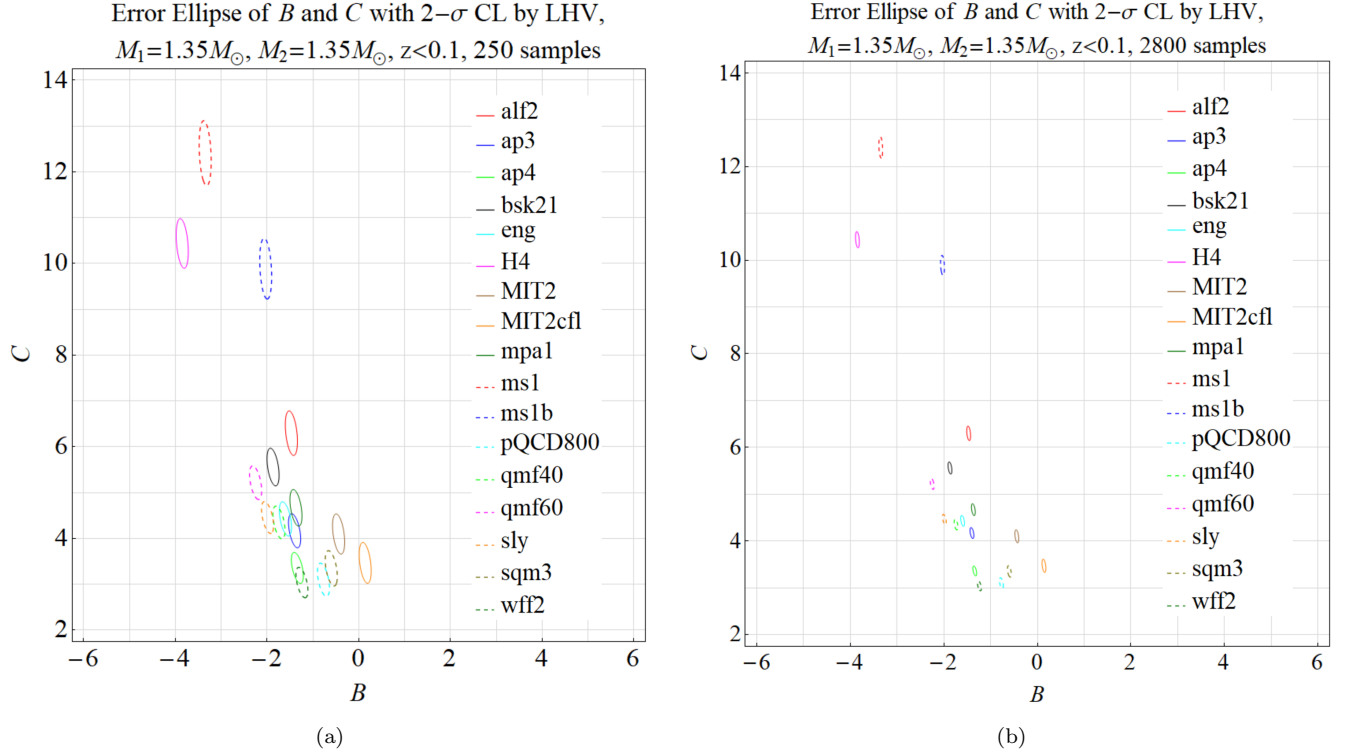


Figure 4. The error ellipses of B and C at $2\text{-}\sigma$ CL for different EOS models under the detection of LHV. We have assumed the EM counterparts for every GW sample are detectable. (a) is plotted with the total 250 samples and (b) is plotted with the total 2800 samples. These samples are generated at $z < 0.1$. The corresponding SNR distributions are illustrated in Fig.3. It is observed that in (a), the error ellipses of ms1, H4, ms1b, alf2, bsk21, qmf60, MIT2, MIT2cfl do not overlap with others, which implies that they are distinguishable by this GW observation. In (b), there is no overlap between any two ellipses, thus in this case all the EOS models are distinguishable.

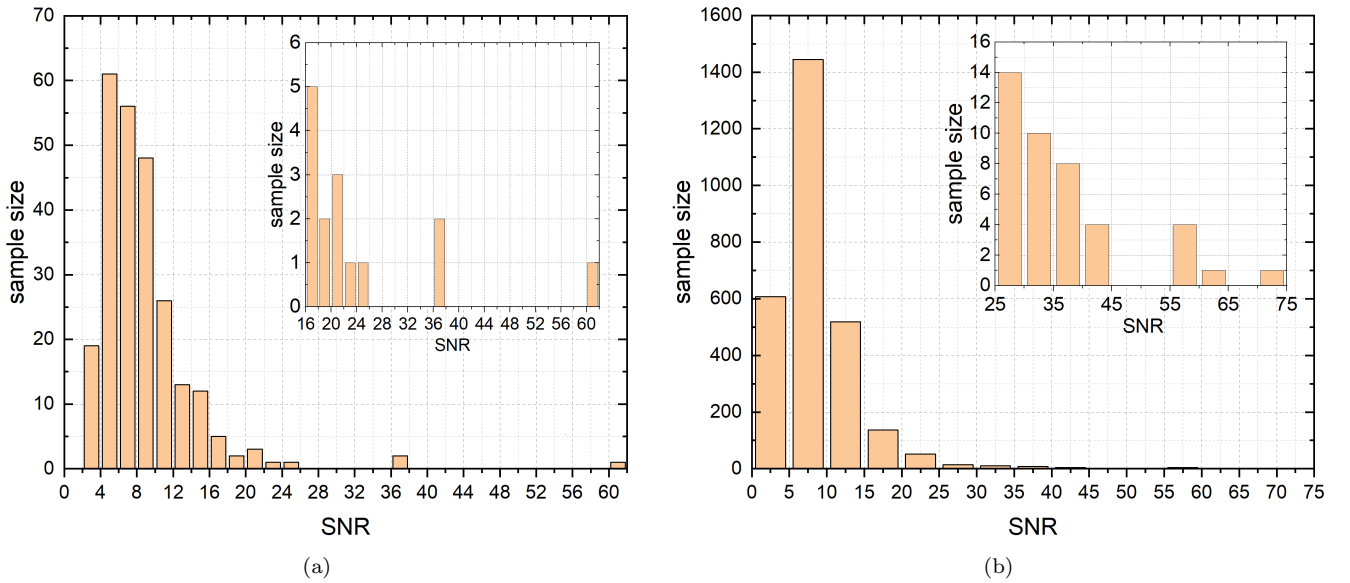


Figure 5. By the detection of LHV, the SNR distribution of the samples generated in the redshift range of $z < 0.1$ is plotted. In (a), there are totally 250 samples and 66 samples are detectable with the threshold of $\text{SNR} > 10$. In (b), there are totally 2800 samples, and 748 samples are detectable.

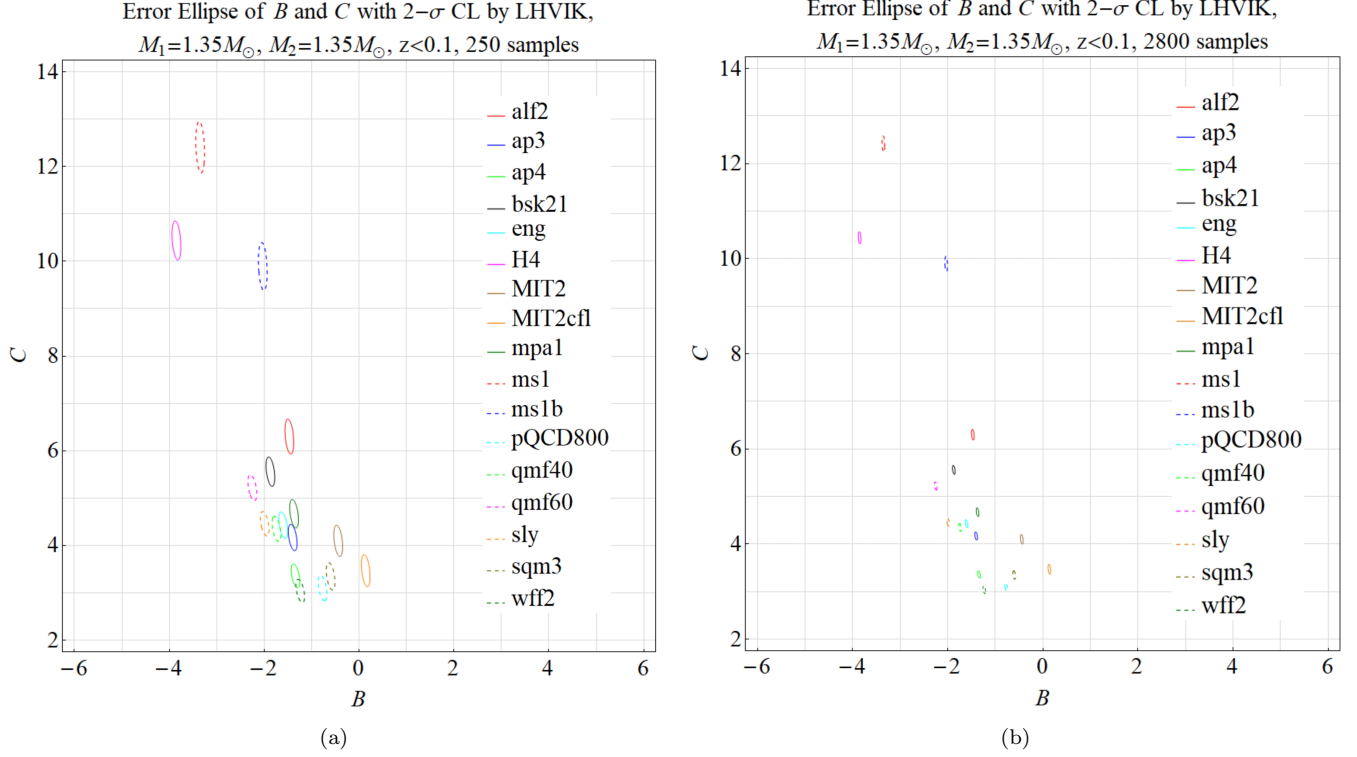


Figure 6. The error ellipses of B and C at $2\text{-}\sigma$ CL for different EOS models under the GW detection of LHVIK. The EM counterparts of all the GW samples are assumed to be detectable. These samples are generated at $z < 0.1$. (a) is plotted with totally 250 samples and (b) is plotted with totally 2800 samples. The corresponding SNR distributions are illustrated in Fig.5. It is observed that in (a), the error ellipses of qmf40, eng, ap4, wff2 have certain overlaps with other models, so that they are indistinguishable by this GW observation. In (b), there is no overlap between any two ellipses, thus in this case all the EOS models are distinguishable.

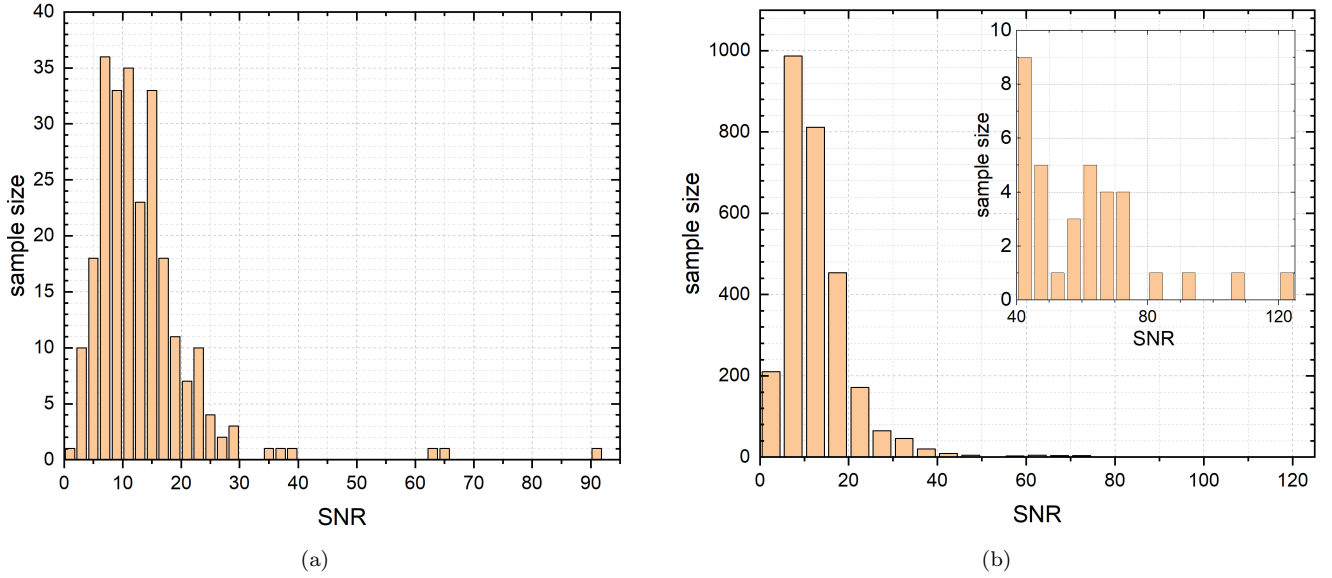


Figure 7. The SNR distribution of the samples generated in the redshift range of $z < 0.1$ detected by 3LA+. With the threshold of $\text{SNR} > 10$, there are 152 detectable samples in the total 250 samples as shown in (a); and there are 1603 detectable samples in the total 2800 samples as shown in (b).

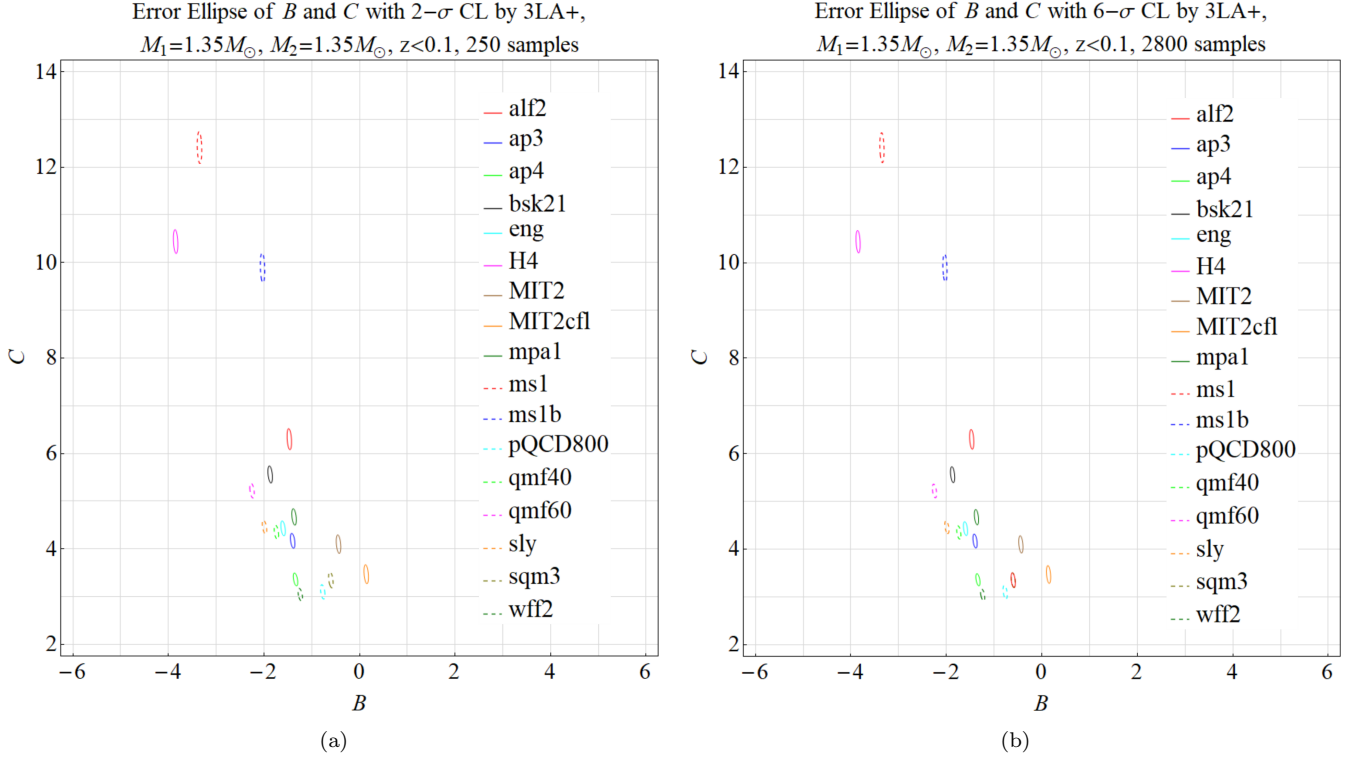


Figure 8. The error ellipses of B and C for different EOS models under the detection of 3LA+. We have assumed the EM counterparts for every GW sample are detectable. (a) is plotted with the total 250 samples and (b) is plotted with the total 2800 samples. These samples are generated at $z < 0.1$, and the corresponding SNR distributions are illustrated in Fig.7. It is observed that in (a) and (b), all the ellipses have no overlap region with the others, so that all the EOS models can be distinguished from each other by 3LA+.

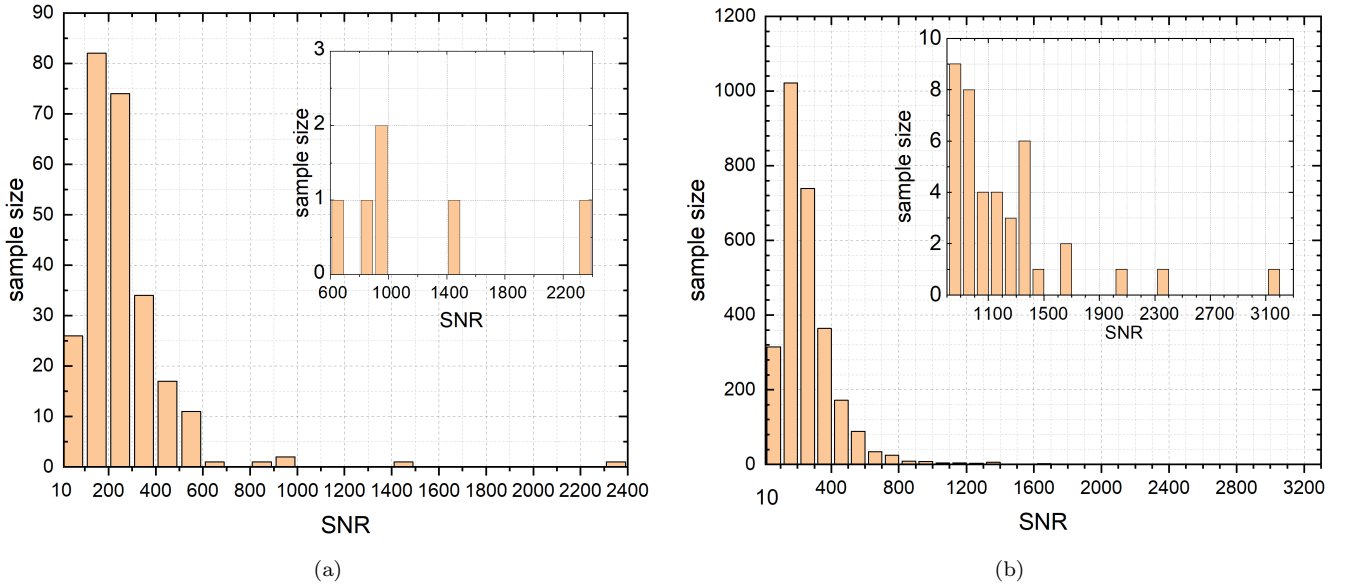


Figure 9. The SNR distribution of the samples generated in the redshift range of $z < 0.1$ detected by ET2CE. There are totally 250 samples in (a), and totally 2800 samples in (b). It is found that with the threshold of $\text{SNR} > 10$, all the GW samples are detectable by ET2CE.

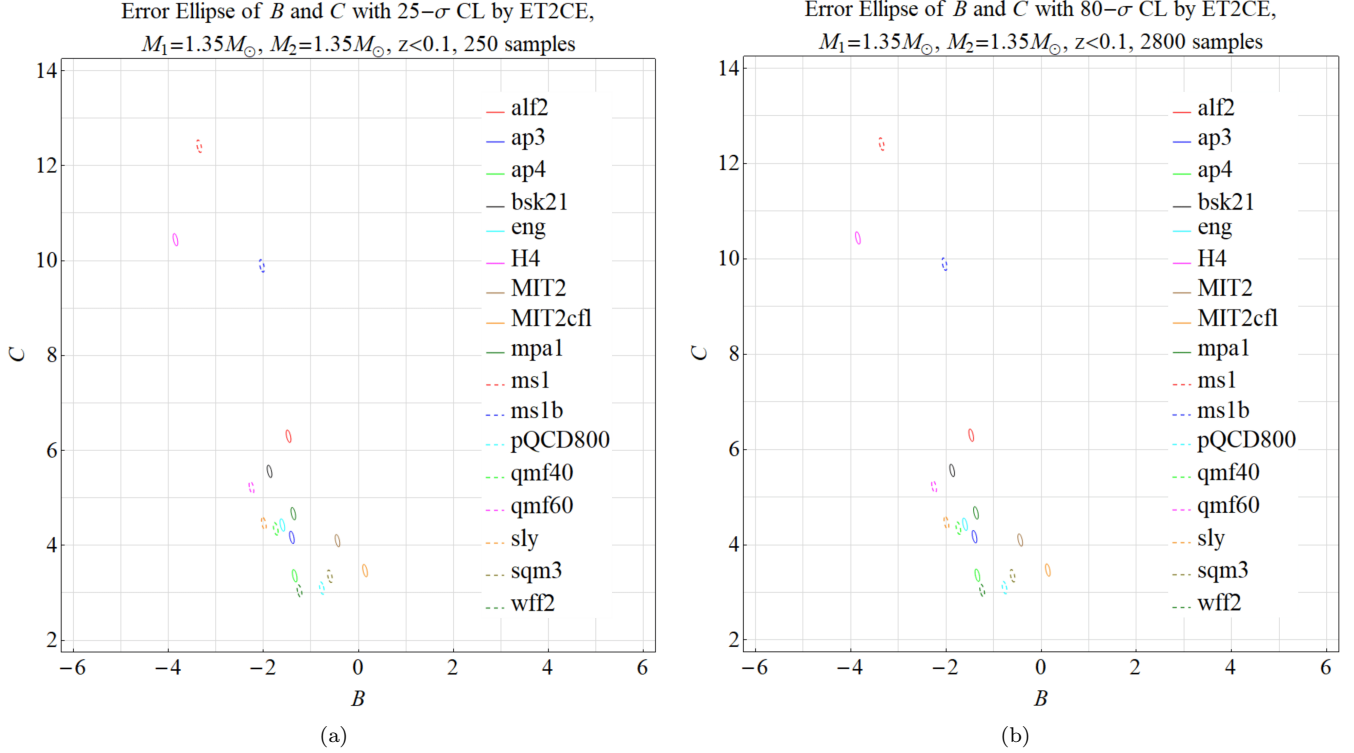


Figure 10. The error ellipses of B and C for different EOS models under the detection of ET2CE. The EM counterparts are assumed to be detectable for every GW sample. (a) is plotted with the total 250 samples, and the error ellipses in (a) are at $25\text{-}\sigma$ CL; (b) is plotted with the total 2800 samples, and the error ellipses in (b) are at $80\text{-}\sigma$ CL. These samples are generated at $z < 0.1$, and the corresponding SNR distributions are illustrated in Fig.9. It is found that all the EOS models are distinguishable by ET2CE and the confidence level is higher than the networks of 2G and 2.5G detectors. These improvements are due to the great sensitivity of the 3G detectors.

in Fig.11 (a). The number of the detectable samples at $z < 0.1$ With the threshold of $\text{SNR} > 10$ for each network is also plotted in Fig.11 (b). It is found that the errors of B and C detected by the 2.5G or 3G detector network are smaller than the 2G one. This is due to the greater sensitivity of the 2.5G and 3G detectors which leads to more detectable samples as shown in Fig.11 (b). And a network with more detectors such as LHVIK can increase the detectable sample size and reduce the errors of B and C but not very significantly.

5.5. Detectable EM counterpart in $z < 0.05$

It is noticed that the second BNS-merger GW event GW190425 is at $z \sim 0.03$, and no EM counterpart is reported (Abbott et al. 2020). Thus, as a more conservative consideration, we assume that in the future, the detectable EM counterpart of the GWs generated by the BNS merger is within the redshift range $z < 0.05$. According to Ref.(Abbott et al. 2019), in a three-year observation, the number of BNS merger events will be 32–370. We repeat a simulation similar to the previous subsections to estimate the error ellipses of the tidal parameters of each EOS model. The SNR distributions by the LHV, LHVIK, 3LA+ and ET2CE networks are plotted in Fig.12, Fig.13, Fig.14 and Fig.15, respectively. Comparing Fig.12 and Fig.3, it can be seen that by LHV, the rate of the detectable samples in $z < 0.05$ and $z < 0.1$ is quite similar. Comparing Fig.13 and Fig.5, it can be seen that by LHVIK, the number of the detectable samples in $z < 0.05$ is greater than that in $z < 0.1$, the same is true for 3LA+ and ET2CE. This is because the detection capability of LHV is weaker than LHVIK, 3LA+ or ET2CE, so the main part of the detectable objects by LHV comes from low redshift. In particular, the number of the detectable samples by LHV is almost unchanged when the redshift is reduced to a lower level. Using these samples, the error ellipses of B and C for different EOS models by using LHV, LHVIK, 3LA+ and ET2CE are presented in Fig.16, Fig.17, Fig.18 and Fig.19, respectively. Comparing Fig.16 and Fig.4, it is observed that the error ellipses obtained in $z < 0.05$ and $z < 0.1$ are similar in size, and the distinguishable EOS models for the two redshift ranges are the same. The error ellipses in Fig.17 by LHVIK

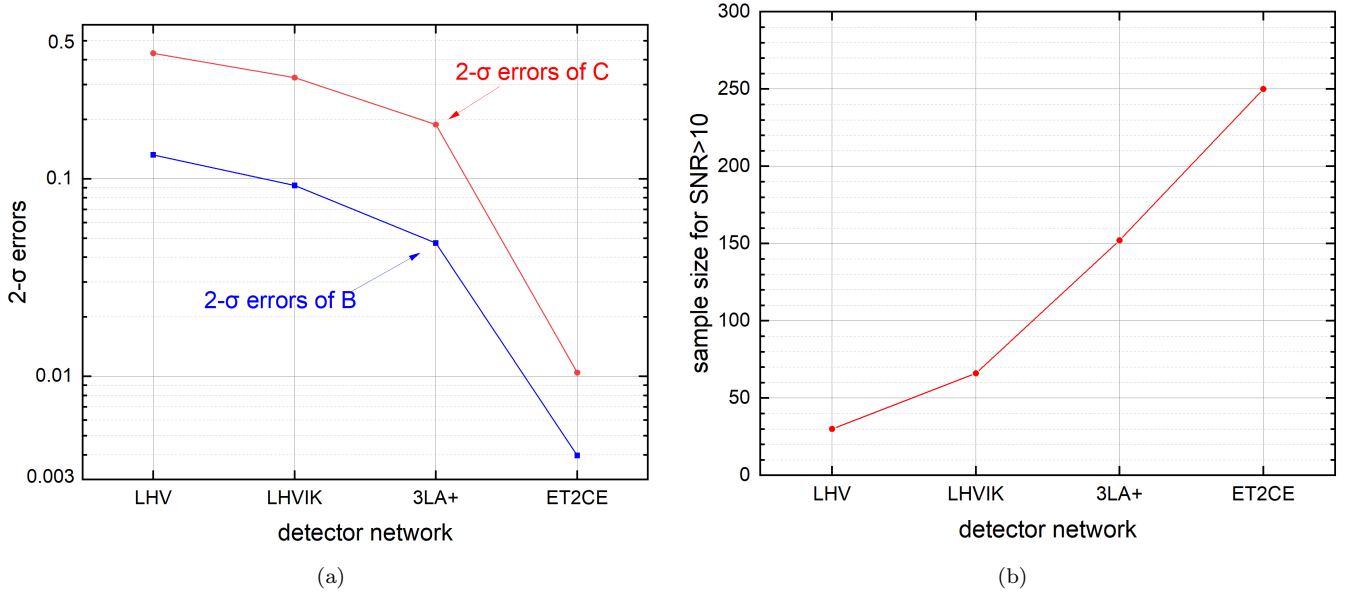


Figure 11. (a) illustrates the average of the 2- σ errors of B and C over all the EOS models for each network, which is calculated with a total of 250 samples at $z < 0.1$. We have assumed the EM counterparts for every GW sample are detectable. (b) illustrates the number of the detectable samples in the redshift range of $z < 0.1$ for each network. It is seen that the detection capability of the 2.5G and 3G detector networks is greater than the 2G ones.

are smaller than in Fig.6, but not significantly, which leads to the same distinguishable EOS models in these two figures. Due to the great sensitivity of ET2CE, in $z < 0.05$ all the EOS models are distinguishable by ET2CE at 20- σ level with totally 32 samples, and at 50- σ level with totally 370 samples. The result for 3LA+ is similar to ET2CE, that using the network of 3LA+, all the EOS models are distinguishable at 2- σ level with totally 32 samples as well as at 4- σ level with totally 370 samples. Therefore, we can conclude that if the redshift range of the detectable EM counterparts is reduced to a smaller but reasonable value, the outcome of the EOS determination still stands.

5.6. No EM counterpart

For comparison, we also consider the case where there is no detectable EM counterpart for each GW signal in a low-redshift range. Under this assumption, the position parameters (θ_s, ϕ_s) and redshift z of the source remain unknown. Subsequently, for each GW event, we need to calculate the Fisher matrix of all 12 parameters, ($\mathcal{M}_c, \eta, t_c, \psi_c, \iota, \theta_s, \phi_s, \psi_s, d_L, z, B, C$), and then marginalize it into a Fisher matrix of two tidal-effect parameters (B, C) as the processing adopted in Sec. 5.1. Then, we sum the Fisher matrices of (B, C) over all detectable GW samples to obtain a total Fisher matrix whose inverse is the covariance matrix of (B, C).

In this subsection, we still consider the redshift range of $z < 0.1$, and the number of BNS-merger events for three-year observation ranges from 250 to 2800. With these setups, we repeat a simulation similar to Sec.5.1, 5.2, 5.3 and 5.4. The distributions for SNR by using LHV, LHVIK, 3LA+ and ET2CE are given in Fig.3, Fig.5, Fig.7, and Fig.9, respectively. The corresponding error ellipses of B and C by using LHV, LHVIK, 3LA+ and ET2CE are plotted in Fig.20, Fig.21, Fig.22 and Fig.23, respectively. If there is no electromagnetic counterpart, in the case of a lower merge rate with 250 samples, when using LHV, all the EOS models are indistinguishable at 1- σ CL; but when using LHVIK, MIT2cfl can be distinguished from other models. When taking a higher merge rate with 2800 samples, the EOS models ms1, H4, ms1b, qmf40, qmf60 can be distinguished by LHV or LHVIK at 1- σ CL, other models are indistinguishable. By 3LA+, at 1- σ CL, with totally 250 samples, the EOS models ms1, H4, MIT2cfl can be distinguished but the others are indistinguishable. While with totally 2800 samples, except for mpa1 and ap3, which have similar prediction of radii and $\lambda - m$ slopes for neutron stars, other EOS models can be distinguished. By ET2CE, all the EOS models are distinguishable, which is the same as the conclusion of previous subsections. Comparing these figures with Fig.4, Fig.6, Fig.8 and Fig.10, it is observed that the errors of B and C are much larger than those with detectable EM counterpart. Thus, EM counterparts are important for the determination of EOS, especially for the networks of 2G and 2.5G detectors.

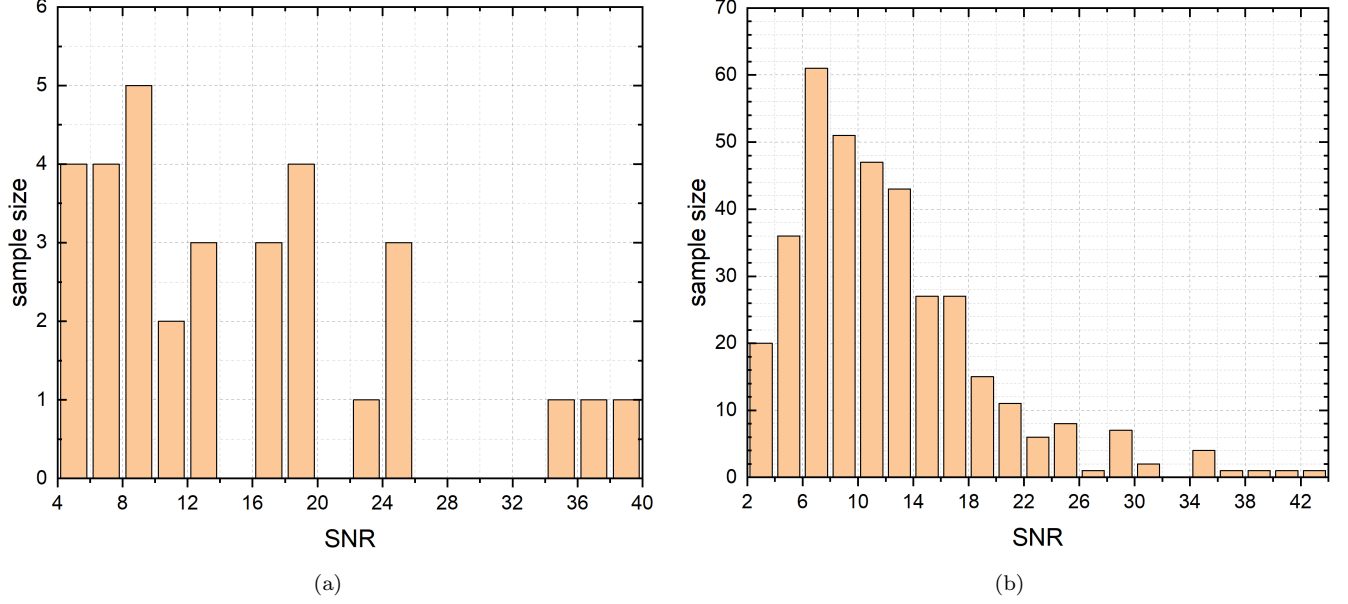


Figure 12. The SNR distribution of the samples generated in the redshift range of $z < 0.05$ detected by LHV. There are totally 32 samples in (a), and totally 370 samples in (b), according to the lowest and highest event rates given in Ref.([Abbott et al. 2019](#)) respectively. It is found that with the threshold of $\text{SNR} > 10$, there are 19 detectable samples in (a), and 202 detectable samples in (b).

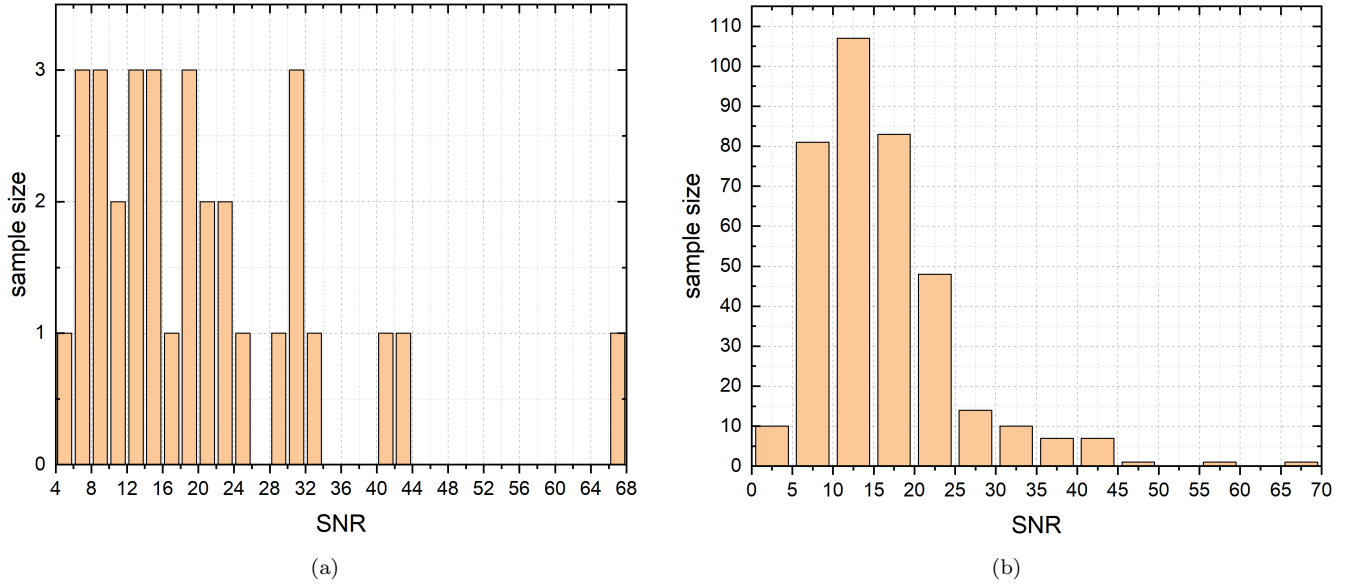


Figure 13. The SNR distribution of the samples generated in the redshift range of $z < 0.05$ detected by LHVik. With the threshold of $\text{SNR} > 10$, there are 25 detectable samples in the total 32 samples as shown in (a); and there are 279 detectable samples in the total 370 samples as shown in (b).

6. DETERMINATION OF DARK ENERGY

Dark energy with positive density but negative pressure is believed to be an impetus of the accelerated expansion of the universe ([Albrecht et al. 2006](#); [Amendola & Tsujikawa 2010](#)), and a large number of dark energy models have been proposed in the literature ([Frieman et al. 2008](#)). In order to differentiate these different models, it is essential to measure the EOS of dark energy. Currently, the main methods include observations of SNIa, CMB, large-scale

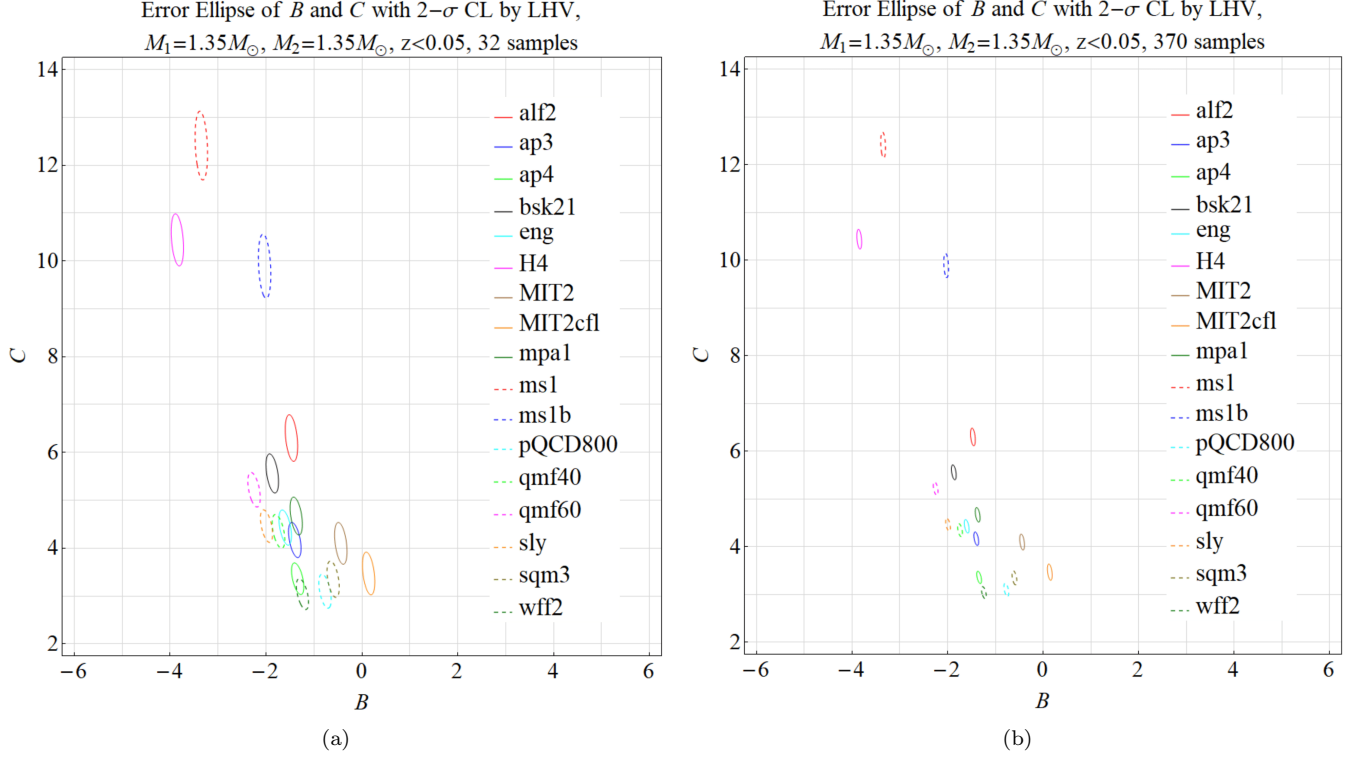


Figure 16. The error ellipses of B and C at $2\text{-}\sigma$ CL for different EOS models under the detection of LHV. (a) is plotted with totally 32 samples and (b) is plotted with totally 370 samples. These samples are generated at $z < 0.05$, and the corresponding SNR distributions are illustrated in Fig.12. We have assumed the EM counterparts for every GW sample are detectable. It is observed that the overlaps between the ellipses as well as the distinguishable EOS models are the same as in Fig.4.

for most high-redshift (*e.g.* $z > 0.1$) events, it is unlikely that the EM counterparts will be observed. In this section, we analyze the GW waveforms containing the tidal effects, from which both redshift and luminosity distance can be obtained. Furthermore, the evolution of dark matter can be studied. For the EOS model of BNS, we will adopt the B and C obtained from GW and the corresponding EM counterpart observations at the low-redshift as a prior condition, and add it to the process of analyzing the dark energy EOS with only GW observation in the high-redshift range.

In order to quantify the EOS of dark energy, in this article, we adopt the widely-used Chevallier-Linder-Polarski parametrization (Chevallier & Polarski 2001; Linder 2003; Albrecht et al. 2006), in which a parameter $w(z)$ is introduced as the ratio of the pressure p_{de} and energy density ρ_{de} of dark energy as

$$w(z) = \frac{p_{\text{de}}}{\rho_{\text{de}}} = w_0 + w_a \frac{z}{1+z}, \quad (17)$$

where w_0 and w_a are two constants. w_0 represents the a present-day value of EOS and w_a represents its evolution with redshift. In the Λ CDM model, a cosmological constant Λ , corresponds to $w_0 = -1$ and $w_a = 0$. In a general Friedmann-Lemaitre-Robertson-Walker (FLRW) universe, the luminosity distance of astrophysical sources is a function of redshift z as (Weinberg 2008)

$$d_L(z) = (1+z) \begin{cases} |k|^{-1/2} \sin \left[|k|^{1/2} \int_0^z \frac{dz'}{H(z')} \right] & (\Omega_k < 0) \\ \int_0^z \frac{dz'}{H(z')} & (\Omega_k = 0) \\ |k|^{-1/2} \sinh \left[|k|^{1/2} \int_0^z \frac{dz'}{H(z')} \right] & (\Omega_k > 0) \end{cases} \quad (18)$$

where Ω_k is the contribution of spatial curvature density, and the Hubble parameter $H(z)$ is

$$H(z) = H_0 \left[\Omega_m (1+z)^3 + \Omega_k (1+z)^2 + (1 - \Omega_m) E(z) \right]^{1/2}, \quad (19)$$

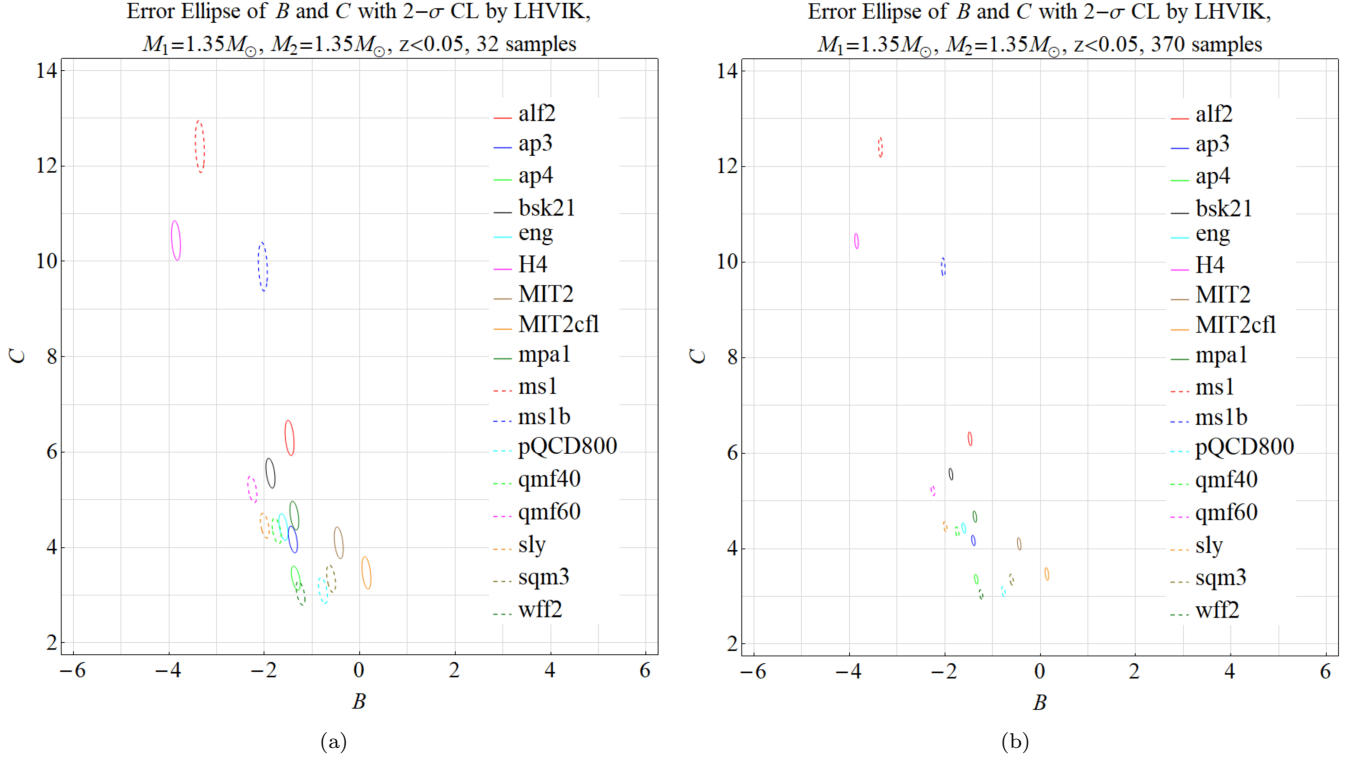


Figure 17. The error ellipses of B and C at $2\text{-}\sigma$ CL for different EOS models under the detection of LHVik. (a) is plotted with totally 32 samples and (b) is plotted with totally 370 samples. These samples are generated at $z < 0.05$, and the corresponding SNR distributions are shown in Fig.13. We have assumed the EM counterparts for every GW sample are detectable. It is observed that the overlaps between the ellipses as well as the distinguishable EOS models are the same as in Fig.6.

with

$$E(z) = (1+z)^{3(1+w_0+w_a)} e^{-3w_a z/(1+z)}. \quad (20)$$

There are five cosmological parameters to be determined in the above d_L - z relation, i.e., $(H_0, \Omega_m, \Omega_k, w_0, w_a)$. However, as Ref.(Zhao et al. 2011) has shown, the background parameters $(H_0, \Omega_m, \Omega_k)$ and the dark energy parameters (w_0, w_a) have strong degeneracy, thus one cannot constrain the full parameters from GW standard sirens alone. The SNIa and BAO methods for dark energy detection also suffer the same problem. A general way to break this degeneracy is to take the CMB constraints for the parameters $(H_0, \Omega_m, \Omega_k)$ as a prior, which is nearly equivalent to treat the three parameters as known in data analysis (Zhao et al. 2011; Zhao & Wen 2018). Therefore, in the following, we only study the constraints on parameters (w_0, w_a) under GW observation. The Fisher matrix of (w_0, w_a) can be obtained by converting the measurement error of d_L as following

$$F_{ij} = \sum_k \frac{(\partial \ln d_L(k)/\partial p_i)(\partial \ln d_L(k)/\partial p_j)}{(\Delta d_L/d_L(k))^2 + (\Delta d'_L/d_L(k))^2 + \sigma_l^2}, \quad (21)$$

where both the indices i and j run from 1 to 2, and (p_1, p_2) indicate two free parameters (w_0, w_a) . The index $k = 1, 2, \dots, N$ labels the event with redshift and position at $(z_k, \theta_{sk}, \psi_{sk})$ in the total N sources. $\sigma_l = 0.05z$ is the contribution of the weak-lensing effect to the error of d_L (Sathyaprakash et al. 2010; Zhao et al. 2011), $\Delta d'_L$ is induced from the redshift error Δz as

$$\Delta d'_L = \frac{\partial d_L(z)}{\partial z} \Delta z. \quad (22)$$

In (21) and (22), Δd_L and Δz are the $1\text{-}\sigma$ errors. To get Δd_L and Δz , we first calculate a 12×12 Fisher matrix from the k -th GW sample of the full 12 parameters $(\mathcal{M}_c, \eta, t_c, \psi_c, \iota, \theta_s, \phi_s, \psi_s, d_L, z, B, C)$ in the redshift range of $0.1 < z < 2$. Then, we add the Fisher matrix of B and C obtained from the low-redshift GW and corresponding EM

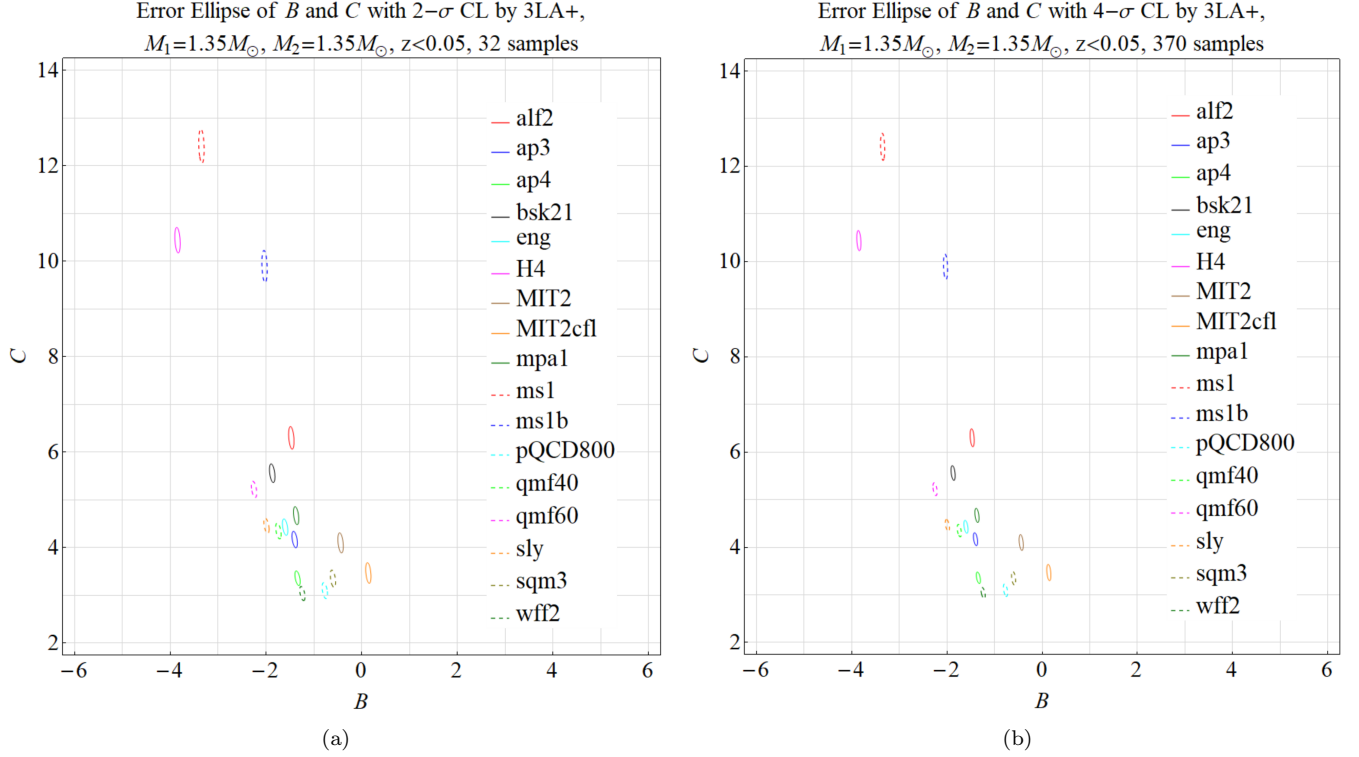


Figure 18. The error ellipses of B and C for different EOS models under the detection of 3LA+. (a) is plotted with totally 32 samples at $2\text{-}\sigma$ CL and (b) is plotted with totally 370 samples at $4\text{-}\sigma$ CL. These samples are generated at $z < 0.05$, and the corresponding SNR distributions are shown in Fig.14. We have assumed the EM counterparts for every GW sample are detectable. It is observed that all the EOS models are distinguishable, but the confidence level in (b) of this figure is lower than that in Fig.8 (b).

counterparts to the B - and C -related elements in this 12×12 Fisher matrix as a prior (Coe 2009). Δd_L and Δz are the square root of the (d_L, d_L) - and (z, z) -diagonal elements of the inverse of this new 12×12 matrix.

There is also another quantity, the figure of merit (FoM) (Albrecht et al. 2006), indicating the goodness of constraints from observational data sets, which is proportional to the inverse area of the error ellipse in the w_0 - w_a plane as following

$$\text{FoM} = [\text{Det } C(w_0, w_a)]^{-1/2}, \quad (23)$$

where $C(w_0, w_a)$ is the covariance matrix of w_0 and w_a . Larger FoM means stronger constraint on the parameters, since it corresponds to a smaller error ellipse.

By adopting the merger rates in Ref.(Abbott et al. 2019), there will be $2.1 \times 10^5 \sim 7.2 \times 10^6$ merger events for three-year observation. And when the number of events is large, the sum of events in Eq.(21) can be replaced by the following integral (Zhao et al. 2011)

$$F_{ij} = N \times \int_0^{z_{\max}} \frac{\partial \ln d_L(z)}{\partial p_i} \frac{\partial \ln d_L(z)}{\partial p_j} f(z) \left\langle \frac{1}{(\Delta d_L/d_L(k))^2 + (\Delta d'_L/d_L(k))^2 + \sigma_l^2} \right\rangle dz, \quad (24)$$

where $f(z)$ is the number distribution of the GW sources over redshift z , and $\langle \dots \rangle$ is the average over the angles $(\theta_s, \phi_s, \iota, \psi_s)$. Thus, the $1\text{-}\sigma$ errors of Δw_0 and Δw_a , and FoM are related to a large number N of the total events as following

$$\Delta w_0 = \frac{A_{w_0}}{\sqrt{N}}, \quad \Delta w_a = \frac{A_{w_a}}{\sqrt{N}}, \quad \text{FoM} = A_{\text{FoM}} N, \quad (25)$$

where the values of the coefficients A_{w_0} , A_{w_a} and A_{FoM} depend on the type of detector network. Eq.(25) makes it easy to convert the estimation errors for one large number of events to another.

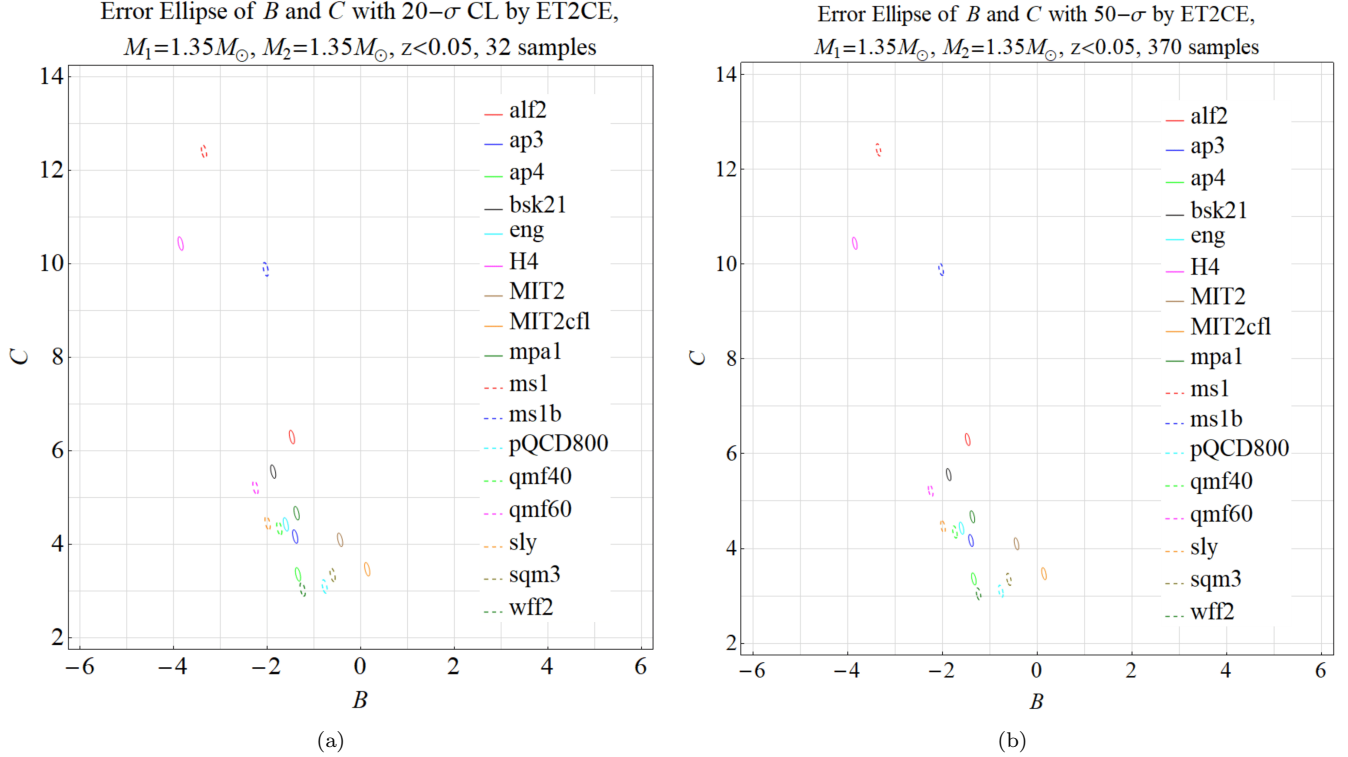


Figure 19. The error ellipses of B and C for different EOS models under the detection of ET2CE. (a) is plotted with totally 32 samples at $20\text{-}\sigma$ CL and (b) is plotted with totally 370 samples at $50\text{-}\sigma$ CL. These samples are generated at $z < 0.05$, and the corresponding SNR distributions are shown in Fig.15. We have assumed the EM counterparts for every GW sample are detectable. It is observed that all the EOS models are distinguishable, but the confidence levels are lower than that in Fig.10.

Since only in the 3G era, a larger number of high-redshift BNSs are expected to be detected by GW observations, in this article, we will focus on the 3G detector network for the determination of dark energy. We perform a simulation to estimate the errors of w_0 and w_a by the ET2CE network. Following Sec.5.4, we also take the assumption that the EM counterparts are detectable only in $z < 0.1$. Thus, at the lowest merger rate, we generate 2.1×10^5 GW samples within the redshift range of $0.1 < z < 2$ numerically, and its SNR distribution is shown in Fig.24 (a), where the number of detectable sample is 1.6×10^5 , accounting for $\sim 76\%$ of the total samples. At the highest merger rate, the SNR distribution with totally 7.2×10^6 GW samples is shown in Fig.24 (a), where the number of detectable sample is 5.5×10^6 , accounting for $\sim 76\%$ of the total samples too. Note that Ref.(Del Pozzo et al. 2017) generated 1000 GW samples and plotted the SNR distribution detected by ET, which showed a $\sim 5\%$ detectable sample proportion under $\text{SNR} > 10$. The difference between these two SNR distributions is due to ET2CE's better detection capability. Taking the Fisher matrix of B and C in Sec.5.4 as a prior, with the total 2.1×10^5 GW samples, we calculate the Fisher matrix (21) for fiducial values $w_0 = -1$ and $w_a = 0$, and yield Δw_0 , Δw_a at $1\text{-}\sigma$ CL for different EOS models, which are listed in Table 3. At the highest merger rate with 7.2×10^6 events, the corresponding Δw_0 , Δw_a and FoM are listed in Table 4. Consistent with the claim in Ref.(Del Pozzo et al. 2017), we find that all the EOSs of NSs yield very similar results. For the case with pessimistic estimation of event rate, GW standard sirens in this method can follow the constraints of $\Delta w_0 \sim 0.004$, $\Delta w_a \sim 0.02$ and $\text{FoM} \sim 4 \times 10^4$. While in the case with optimistic estimation of event rate, the constraints are improved to $\Delta w_0 \sim 0.0006$, $\Delta w_a \sim 0.004$ and $\text{FoM} \sim 2 \times 10^6$.

As a continuation of the discussion in Sec.5.5, we also assume that the detectable EM counterparts are only distributed within $z < 0.05$. Repeating the similar numerical simulation process as previous under this assumption, we find that the errors of w_0 and w_a , and the FoM values are totally the same as in Table 3 and Table 4. This result is conceivable from the results in Sec.5.5, which shows that there is no significant difference between these two redshift ranges in the determination of the EOS model.

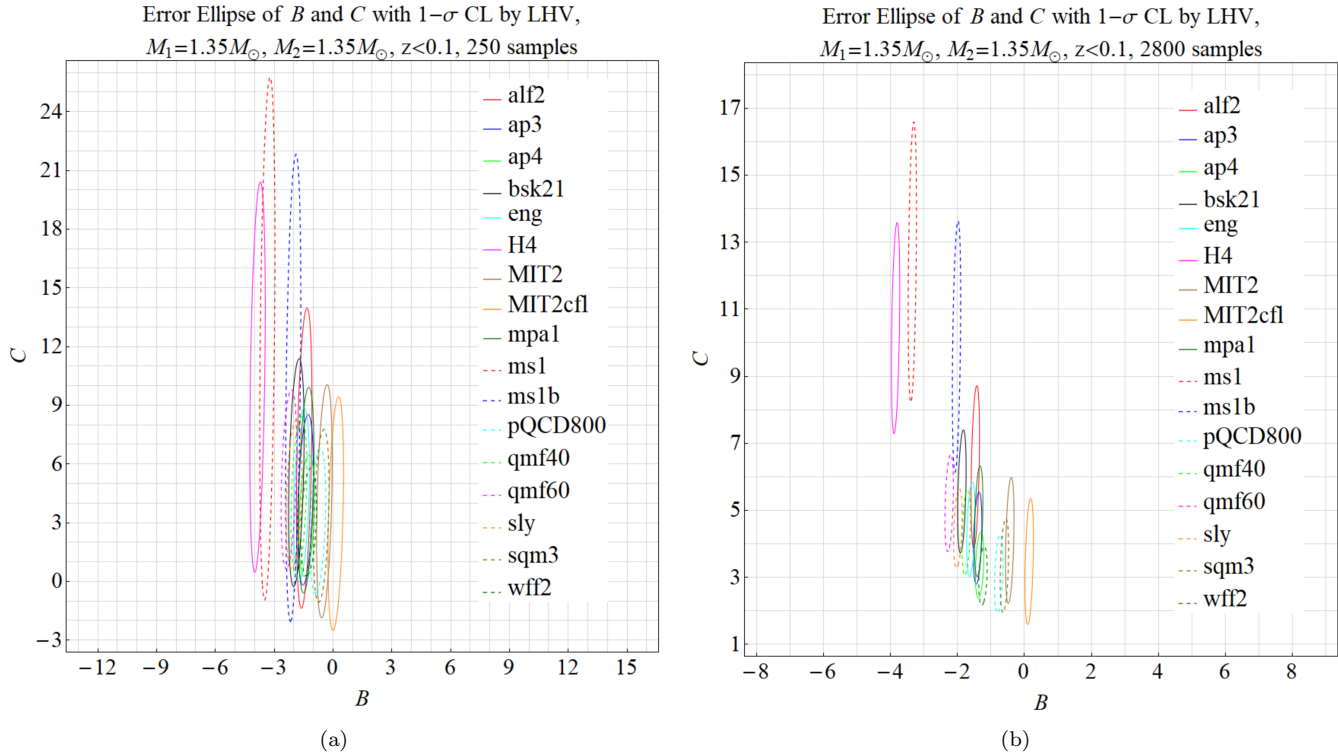


Figure 20. The error ellipses of B and C for different EOS models at $1-\sigma$ CL under the detection of LHV. (a) is plotted with totally 250 samples and (b) is plotted with totally 2800 samples, which are generated at $z < 0.1$ and correspond to the lowest and highest merger rates of BNS (Abbott et al. 2019). The corresponding SNR distributions are the same as that in Fig.3. We have assumed the EM counterparts cannot be detected in these two figures. It is observed that these EOS models are indistinguishable in (a), and there are only the models of ms1, H4, ms1b, qmf40, qmf60 can be distinguished in (b).

To investigate the importance of the observation of EM counterparts, we shall consider a situation that there is no detectable EM counterparts at low redshift. Similar numerical simulation process as previous yields the values of Δw_0 , Δw_a and FoM for each EOS model, which are listed in Table 5 and Table 6. Comparing with Table 5 and Table 3, it is observed that with no EM counterparts, the errors Δw_0 and Δw_a become significantly larger. Therefore, detectable EM counterparts at low redshift can reduce the errors of w_0 and w_a to a certain extent.

It is important to compare our results with those in previous works. Table III in Ref.(Del Pozzo et al. 2017) listed the errors of w_0 and w_a which are determined by a single ET through Bayesian approach. The $1-\sigma$ errors of w_0 and w_a for 2.1×10^5 GW events can be derived from Table III of Ref.(Del Pozzo et al. 2017) as $\Delta w_0 = 0.028$ and $\Delta w_a = 0.031$, which are larger than our results in Table 3. This is mainly due to the better sensitivity of ET2CE network than a single ET. More importantly, Ref.(Del Pozzo et al. 2017) assumed the EOS of NS are known in advance. In this article, we consider a more realistic case, in which we assume the EOS of NSs will be determined by the BNS events at low redshifts with both GW and EM observations. We find that, in 3G era, this approach is nearly equivalent to the case with known NS's EOS, and the assumption in Ref.(Del Pozzo et al. 2017) is justified in our analysis.

In most previous works, the authors investigate the potential constraint of dark energy by GW standard sirens based on the assumption that the high-redshift BNS events have detectable shGRB counterparts. Due to the difficulty of EM observations, the available event number is always to be ~ 1000 in the 3G detection era (Sathyaprakash et al. 2010; Zhao et al. 2011; Cai & Yang 2017; Zhao & Wen 2018), which is justified in our recent simulations (Yu et al. 2020b). In this approach, the potential constraints of dark energy parameters by various 3G detector networks have been explicitly studied in our previous work (Zhao & Wen 2018). For instance, the detector network, including 3 CE-like detectors, is expected to give the constraints of $\Delta w_0 \sim 0.03$ and $\Delta w_a \sim 0.2$, if assuming 1000 face-on BNSs at $z < 2$ have the detected EM counterparts. In comparison with these results, we find that GW standard sirens with tidal effect have a much stronger detection ability for dark energy, which might guide the research direction in this issue.

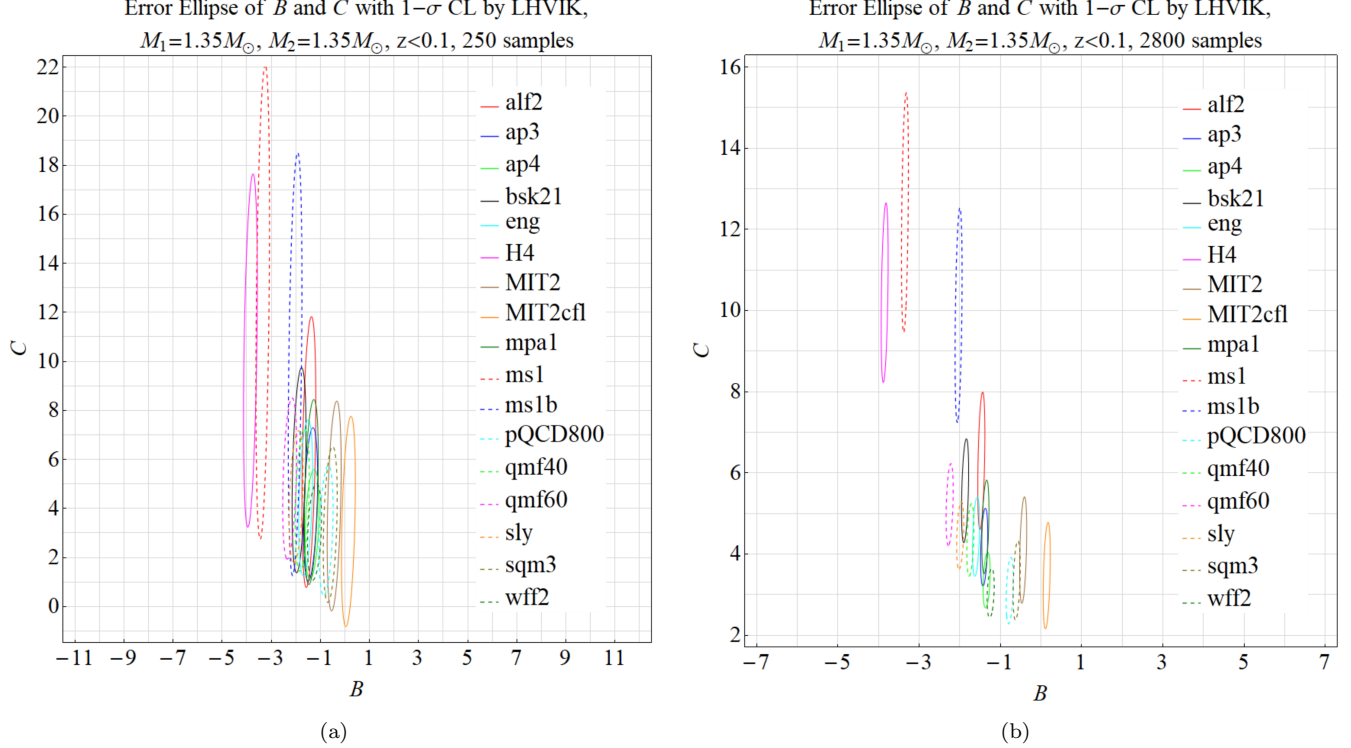


Figure 21. The error ellipses of B and C for different EOS models at $1-\sigma$ CL under the detection of LHVik. (a) is plotted with totally 250 samples and (b) is plotted with totally 2800 samples. The samples are generated at $z < 0.1$, and the corresponding SNR distributions are the same as that in Fig. 5. We have assumed the EM counterparts cannot be detected in these two figures. It is observed that MIT2cfl is distinguishable in (a), and though the error ellipses in (b) are smaller than that in Fig. 20 (b), the distinguishable models in (b) are the same as Fig. 20 (b).

The most recent determination by Planck+SNIa+BAO of the parameters w_0 and w_a reports $\Delta w_0 \sim 0.077$ and $\Delta w_a \sim 0.3$ (Aghanim et al. 2018), which are much larger than our results. In the next generation of SNIa and BAO observations, with the CMB priors, the potential constraints on the dark energy parameters are around $\Delta w_0 \sim 0.03$ and $\Delta w_a \sim 0.1$ (Bock et al. 2006). Therefore, in comparison with the tradition EM methods, we find that in 3G era with GW standard sirens, the constraints on dark energy parameters would be able to improve by 1-3 orders in magnitude. This is mainly attributed to much larger event number of GW sources. So, we conclude that in the near future, the GW standard sirens provide a much more powerful tool for constraining the cosmological parameters.

7. CONCLUSIONS

In this paper, we study the potential detection of the NS's EOS by using the 2G, 2.5G and 3G detectors to detect the GW with corresponding EM in the low redshift under the framework of Fisher matrix analysis. We also study the potential of using 3G detector network with GW from BNS merger as a cosmological probe to determine the dark energy parameters. Specifically, we fit the relation between the tidal deformation λ and the NS mass m around $m = 1.35M_\odot$ by a linear approximation $\lambda = Bm + C$, and choose the parameters B and C to represent different EOS models. At low redshift, the detectable EM counterparts can give the accurate redshift and position of the GW sources. With this, we estimate the errors of B and C by using the tidal effect in GW observation, and propose to use the overlap of two error ellipses of B and C to study the ability of distinguishing different EOS models, which is different from other papers in literature that only set constraints on λ (Hinderer et al. 2010; Abbott et al. 2017a, 2020). Using the EOS model determined by the low redshift as a prior, the GW events of BNS mergers from high redshift can be used as a standard siren to determine its luminosity distance and redshift, which can be used to constrain the dark energy parameters.

According to the BNS merger rate given by Ref. (Abbott et al. 2019), for a 3-year duration of observation, we simulate and generate 250 and 2800 events within the low redshift $z < 0.1$, respectively. With the tidal effect in GW from

Table 3. With the total 2.1×10^5 BNS samples in $0.1 < z < 2$, Δw_0 , Δw_a and FoM at $1\text{-}\sigma$ CL are listed in this table for each EOS model derived by ET2CE under a detectable criterion $\text{SNR} > 10$. We use the Fisher matrix of B and C for a total of 250 samples given in Sec.5.4 as a prior.

EOS	Δw_0	Δw_a	FoM
alf2	0.0037	0.021	59619
ap3	0.0041	0.022	54936
ap4	0.0044	0.024	50295
bsk21	0.0039	0.021	58548
eng	0.0041	0.022	55503
H4	0.0035	0.020	63756
mpa1	0.0040	0.022	56784
ms1	0.0034	0.019	63756
ms1b	0.0035	0.020	62097
qmf40	0.0041	0.022	54726
qmf60	0.0040	0.022	57204
sly	0.0042	0.023	54390
wff2	0.0046	0.024	48174
MIT2*	0.0039	0.021	56280
MIT2cfl*	0.0040	0.022	55377
pQCD800*	0.0043	0.023	51681
sqm3*	0.0041	0.022	53634

* These are the EOS models of quark stars.

Table 4. Same with Table 3, but here we consider the optimal event rate with totally 7.2×10^6 BNS samples in $0.1 < z < 2$.

EOS	Δw_0	Δw_a	FoM
alf2	0.00064	0.0035	2.04408×10^6
ap3	0.00070	0.0038	1.88352×10^6
ap4	0.00076	0.0040	1.72440×10^6
bsk21	0.00066	0.0036	2.00736×10^6
eng	0.00070	0.0038	1.90296×10^6
H4	0.00060	0.0033	2.18592×10^6
mpa1	0.00068	0.0037	1.94688×10^6
ms1	0.00058	0.0033	2.18592×10^6
ms1b	0.00060	0.0033	2.12904×10^6
qmf40	0.00071	0.0038	1.87632×10^6
qmf60	0.00069	0.0037	1.96128×10^6
sly	0.00072	0.0038	1.86480×10^6
wff2	0.00078	0.0041	1.65168×10^6
MIT2*	0.00067	0.0037	1.92960×10^6
MIT2cfl*	0.00068	0.0037	1.89864×10^6
pQCD800*	0.00073	0.0039	1.77192×10^6
sqm3*	0.00071	0.0038	1.83888×10^6

* These are the EOS models of quark stars.

Table 5. With totally 2.1×10^5 BNS samples in $0.1 < z < 2$, the values of Δw_0 , Δw_a and FoM at $1\text{-}\sigma$ CL under the detection of ET2CE are listed in this table. We assume there is no detectable EM counterparts at low redshift.

EOS	Δw_0	Δw_a	FoM
alf2	0.0067	0.034	29715
ap3	0.0061	0.031	33369
ap4	0.0062	0.032	31269
bsk21	0.0062	0.032	36246
eng	0.0061	0.031	33495
H4	0.0070	0.037	20055
mpa1	0.0062	0.031	34986
ms1	0.0057	0.030	32571
ms1b	0.0063	0.034	25389
qmf40	0.0062	0.031	32886
qmf60	0.0061	0.031	33705
sly	0.0062	0.032	32466
wff2	0.0063	0.032	30492
MIT2*	0.0063	0.032	36372
MIT2cf*	0.0063	0.032	36372
pQCD800*	0.0062	0.032	32319
sqm3*	0.0061	0.031	33474

* These are the EOS models of quark stars.

Table 6. Same with Table 5, but here we consider the optimal event rate with totally 7.2×10^6 BNS samples in $0.1 < z < 2$.

EOS	Δw_0	Δw_a	FoM
alf2	0.00115	0.0057	1.01880×10^6
ap3	0.00105	0.0054	1.14408×10^6
ap4	0.00107	0.0055	1.07208×10^6
bsk21	0.00107	0.0054	1.24272×10^6
eng	0.00105	0.0054	1.14840×10^6
H4	0.00119	0.0063	0.68760×10^6
mpa1	0.00105	0.0054	1.19952×10^6
ms1	0.00097	0.0051	1.11672×10^6
ms1b	0.00108	0.0058	0.87048×10^6
qmf40	0.00105	0.0054	1.12752×10^6
qmf60	0.00104	0.0054	1.15560×10^6
sly	0.00105	0.0054	1.11312×10^6
wff2	0.00108	0.0055	1.04544×10^6
MIT2*	0.00107	0.0054	1.24704×10^6
MIT2cf*	0.00107	0.0054	1.24704×10^6
pQCD800*	0.00105	0.0054	1.10808×10^6
sqm3*	0.00105	0.0054	1.14768×10^6

* These are the EOS models of quark stars.

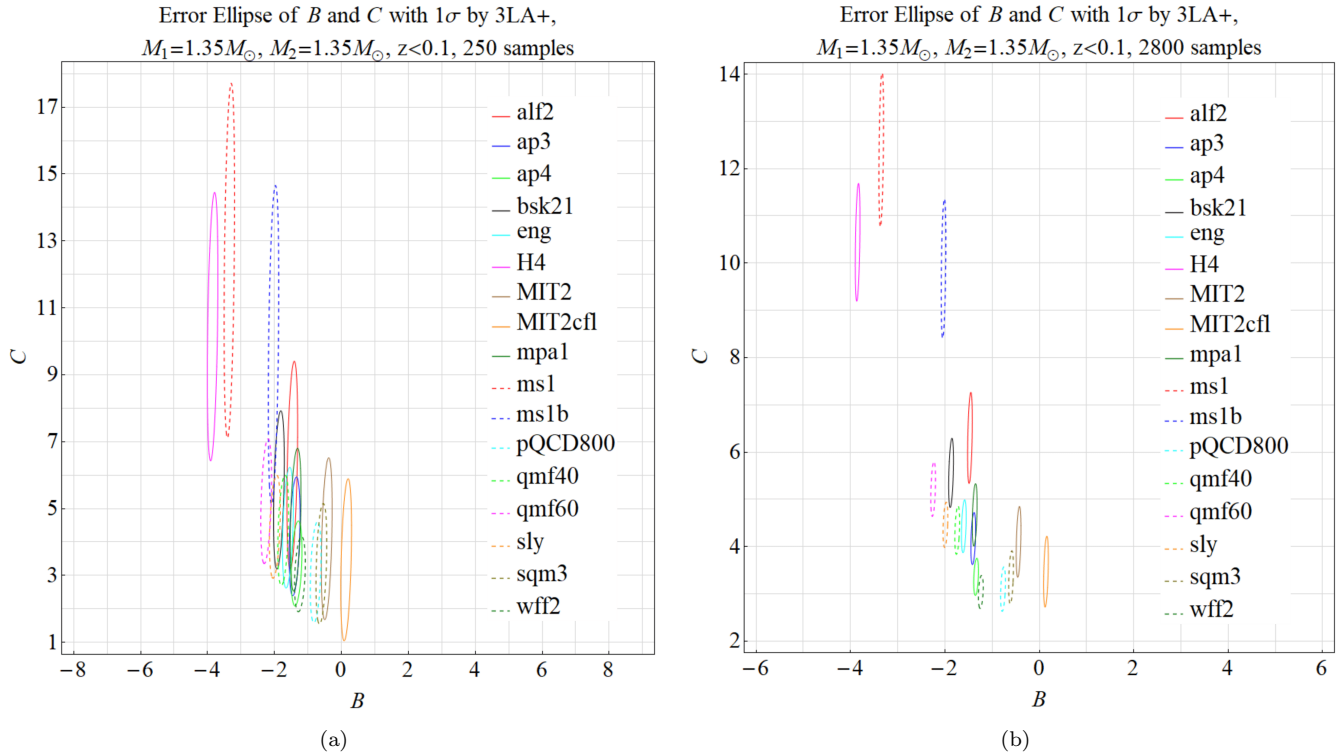


Figure 22. The error ellipses of B and C for different EOS models at $1\text{-}\sigma$ CL under the detection of 3LA+. (a) is plotted with totally 250 samples and (b) is plotted with totally 2800 samples. The samples are generated at $z < 0.1$, and the corresponding SNR distributions are the same as that in Fig.7. We have assumed the EM counterparts cannot be detected in these two figures. It is observed that ms1, H4, MIT2cfl can be distinguished in (a), and except for mpal and ap3, the other EOS models can be distinguished in (b).

BNS merger, under the Fisher matrix analysis, we compare the capability of distinguishing EOS models by different 2G, 2.5G, and 3G detectors. The main result of the study is that, at the $2\text{-}\sigma$ CL, if EM counterparts are detectable at low redshift, when the merge rate of BNS is taken as the upper limit of the theoretical value, the 2G detector networks can distinguish all the 17 EOS models adopted in this paper. While, if the merge rate is taken as its lower limit, most EOS models can be distinguished by the 2G detector networks, but there are still some indistinguishable EOS models. For any merger rate in the theoretical range, the 2.5G and 3G detector networks can distinguish all these EOS models due to their great sensitivity. We also check that if the detectable EMs lie in the redshift range of $z < 0.05$, the above results still hold. To emphasize the importance of detectable EM, we have taken the assumption that there is no EM detectable at the low redshift as shown in Sec. 5.6. The result shows that in the given range of merger rate, none of the 17 EOS models can be distinguished by the 2G detector networks, some of the EOS models can be distinguished by the 2.5G detector networks, and only the 3G detector networks will be able to distinguish all the 17 EOS models. Thus, EM counterparts are important for the determination of EOS, especially for the networks of 2G and 2.5G detectors.

It needs to be noticed that the above conclusions are based on the assumption that all merging NSs have the same mass as $1.35M_\odot$. The actual merging NS masses are more likely to be different. As discussed at the end of Sec. 5.1, different NS masses will not significantly affect the differentiation of the EOS models under the approximated NS mass-distribution adopted in this paper. However, the true mass-distribution remains unknown. Therefore, to distinguish EOS models with more realistic mass-distribution requires more careful analysis in the future.

With the EOS model determined in low redshift by ET2CE as a prior, and considering tidal effect, we calculate the errors of redshift and luminosity distance of GW sources by only using the GW observation from the high-redshift range $0.1 < z < 2$ by ET2CE. Then, we convert these errors into the errors of parameters of dark matter w_0 and w_a according to Eq.(21). The results are listed in Table 3 and Table 4 for the lowest and highest merger rate respectively. We have shown that our results are consistent with Ref.(Zhao & Wen 2018; Del Pozzo et al. 2017), and the future

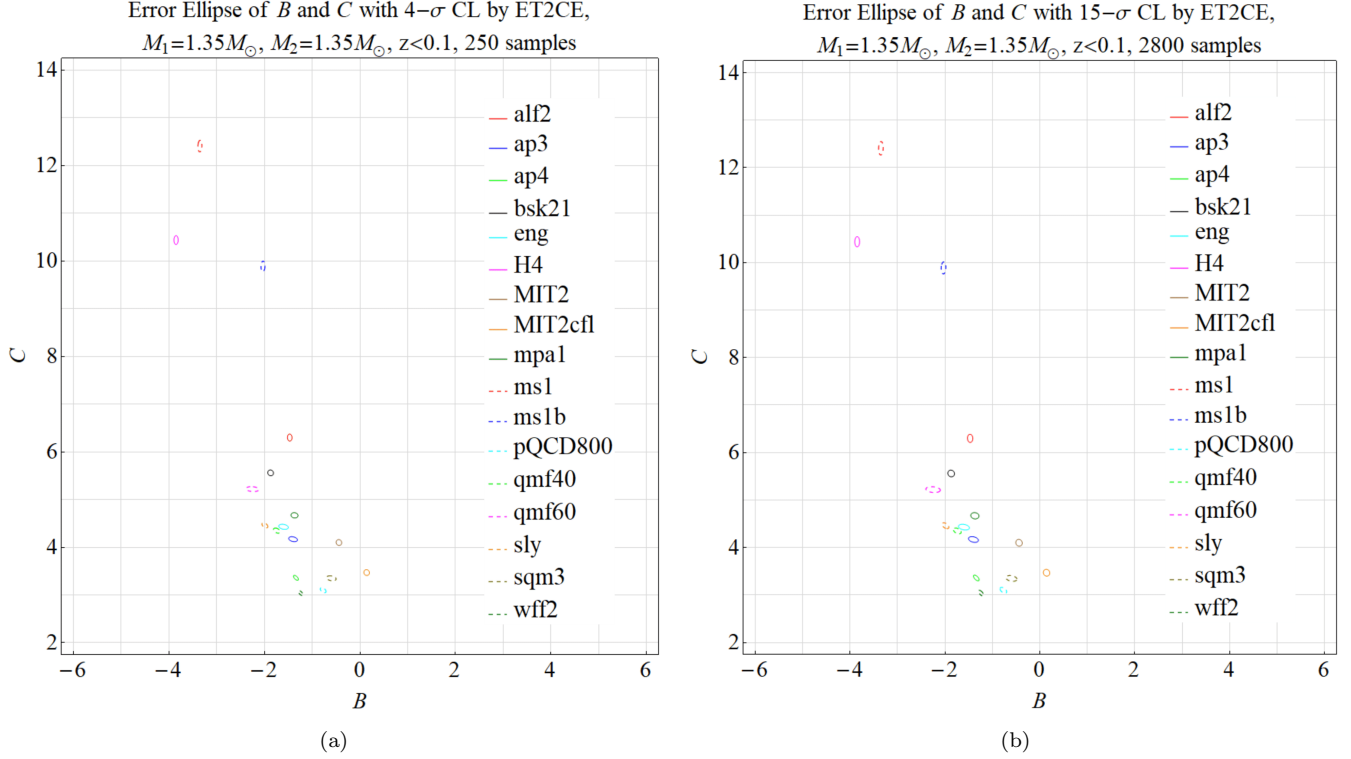


Figure 23. The error ellipses of B and C for different EOS models under the detection of ET2CE. (a) is plotted at $4\text{-}\sigma$ CL with totally 250 samples and (b) is plotted at $15\text{-}\sigma$ CL with totally 2800 samples. The samples are generated at $z < 0.1$, and the corresponding SNR distributions are the same as that in Fig.9. We have assumed the EM counterparts cannot be detected in these two figures. It is observed that all the EOS models are distinguishable. However, the confidence levels are smaller than that in Fig.10.

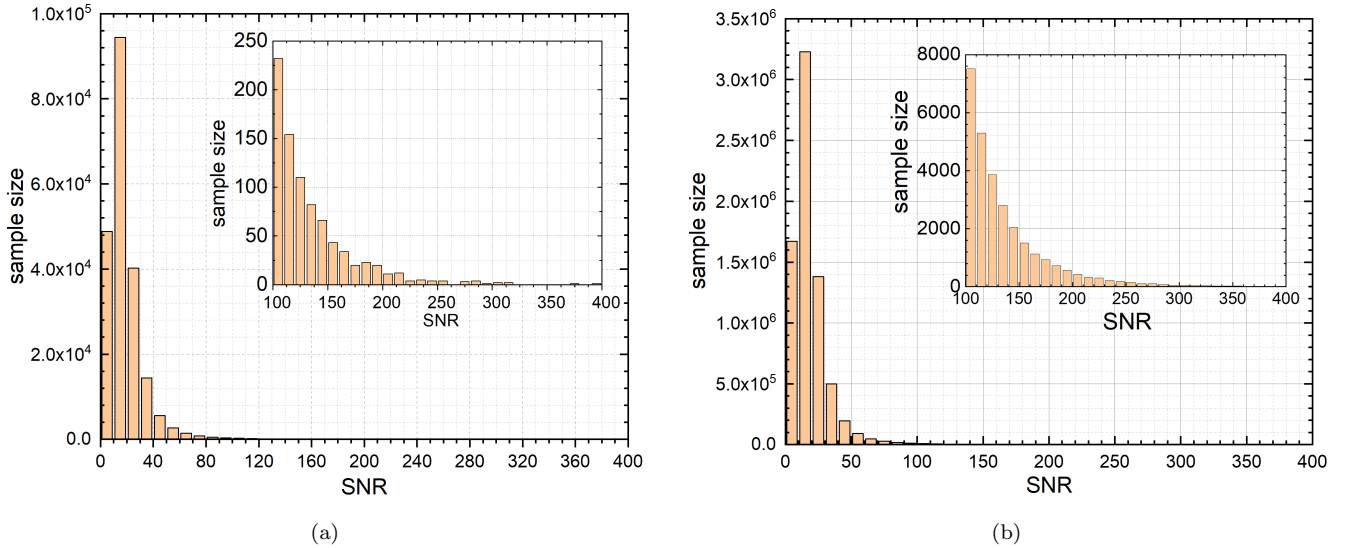


Figure 24. The SNR distribution of the samples generated in the redshift range of $0.1 < z < 2$ detected by ET2CE. According to the lowest and highest event rates given in Ref.(Abbott et al. 2019), we generate a total of 2.1×10^5 and 7.2×10^6 samples in (a) and (b) respectively. With the threshold of $\text{SNR} > 10$, 1.6×10^5 samples are detectable in (a), and 5.5×10^6 samples are detectable in (b). The detectable samples account for $\sim 76\%$ of the total samples in both (a) and (b).

GW observation shall give better constraints on w_0 and w_a than the CMB observation (Aghanim et al. 2018). We also calculate the errors of w_0 and w_a with no EM counterparts at low redshift, which are listed in Table 5 and Table 6. It is seen that without EM counterparts, the errors of w_0 and w_a become significantly larger.

In our analysis, for simplicity, we neglect the NS spins, which is believed to be small in BNS systems (O’Shaughnessy & Belczynski 2008). In addition, we only consider the post-Newtonian expansion at the inspiral stage of BNS merger, which has been proved to be in good agreement with observations (Abbott et al. 2017a, 2020). We have also made a strong assumption in our analysis that the EOS of all neutron stars is the same, which allows us to refer to the EOS parameters obtained from the low redshift to the high redshift for constraining parameters of dark energy. But in reality, neutron stars may have different EOS depending on the internal material composition. For example, the EOS of a quark star and a neutron star are likely to be different (Arroyo-Chvez et al. 2020; Weber et al. 2012). We shall leave this problem in our future research.

Acknowledgements

We appreciate the helpful discussions with Yong Gao and Lijing Shao. This work is supported by the China Postdoctoral Science Foundation grant No. 2019M662168, NSFC Grants Nos. 11773028, 11603020, 11633001, 11873040, and the Strategic Priority Research Program of the Chinese Academy of Sciences Grant No. XDB23010200.

REFERENCES

- Aasi, J., Abbott, B. P., & Abbott, R. 2015, *Class. Quant. Grav.*, 32, 074001
- Abbott, B. P., Abbott, R., Abbott, T. D., et al. 2016a, *Physical review letters*, 116, 061102
- . 2016b, *Physical Review D*, 93, 122003
- . 2016c, *Physical Review Letters*, 116, 241102
- . 2016d, *Physical Review Letters*, 116, 131103
- . 2016e, *The Astrophysical journal letters*, 826, L13
- . 2016f, *The Astrophysical Journal Supplement Series*, 225, 8
- . 2016g, *Physical Review D*, 94, 064035
- . 2016h, *Living Reviews in Relativity*, 19, 1
- . 2017a, *Physical Review Letters*, 119, 161101
- . 2017b, *Nature*, 551, 85
- . 2017c, *The Astrophysical Journal*, 848, L12
- . 2017d, *Classical and Quantum Gravity*, 34, 044001
- . 2018a, *Physical review letters*, 121, 161101
- . 2018b, *Living Reviews in Relativity*, 21, 3
- . 2019, *Physical Review X*, 9, 031040
- . 2020, *The Astrophysical Journal*, 892, L3
- Abdelsalhin, T., Gualtieri, L., & Pani, P. 2018, *Physical Review D*, 98, 104046
- Acernese, F., Agathos, M., Agatsuma, K., et al. 2014, *Classical and Quantum Gravity*, 32, 024001
- Aghanim, N., Akrami, Y., Ashdown, M., et al. 2018, arXiv preprint arXiv:1807.06209
- Albrecht, A., Bernstein, G., Cahn, R., et al. 2006, *astro-ph/0609591*
- Amendola, L., & Sellentin, E. 2016, *Monthly Notices of the Royal Astronomical Society*, 457, 1490
- Amendola, L., & Tsujikawa, S. 2010, *Dark energy: theory and observations* (Cambridge University Press)
- Antoniadis, J., Freire, P. C. C., Wex, N., et al. 2013, *Science*, 340, 1233232
- Arroyo-Chvez, G., Cruz-Osorio, A., Lora-Clavijo, F. D., Campuzano Vargas, C., & Garca Mora, L. A. 2020, *Astrophysics and Space Science*, 365, 43
- Arzoumanian, Z., Brazier, A., Burke-Spolaor, S., et al. 2018, *The Astrophysical Journal Supplement Series*, 235, 37
- Aso, Y., Michimura, Y., Somiya, K., et al. 2013, *Physical Review D*, 88, 043007
- Banihashemi, B., & Vines, J. 2020, *Physical Review D*, 101, 064003
- Barsotti, L., McCuller, L., Evans, M., & Fritschel, P. 2018, *The A+ design curve* (Tech. Rep. LIGO-T1800042)
- Bini, D., Damour, T., & Faye, G. 2012, *Physical Review D*, 85, 124034
- Blanchet, L., & Iyer, B. R. 2005, *Physical Review D*, 71, 024004
- Bock, J., Church, S., Devlin, M., et al. 2006, *astro-ph/0604101*
- Cai, R.-G., & Yang, T. 2017, *Physical Review D*, 95, 044024
- Chen, H.-Y., Fishbach, M., & Holz, D. E. 2018, *Nature*, 562, 545
- Chevallier, M., & Polarski, D. 2001, *International Journal of Modern Physics D*, 10, 213
- Chu, Q., Wen, L., & Blair, D. 2012, *Journal of Physics: Conference Series*, 363, 012023
- Coe, D. 2009, arXiv preprint arXiv:0906.4123

- Cowperthwaite, P., Villar, V., Scolnic, D., & Berger, E. 2019, *The Astrophysical Journal*, 874, 88
- Cramér, H. 1946, *Mathematical Methods of Statistics* (Princeton University Press, Princeton, N.J.)
- Cromartie, H. T., Fonseca, E., Ransom, S. M., et al. 2020, *Nature Astronomy*, 4, 72
- Cutler, C., Apostolatos, T. A., Bildsten, L., et al. 1993, *Physical Review Letters*, 70, 2984
- Del Pozzo, W., Li, T. G., Agathos, M., Van Den Broeck, C., & Vitale, S. 2013, *Physical review letters*, 111, 071101
- Del Pozzo, W., Li, T. G. F., & Messenger, C. 2017, *Physical Review D*, 95, 043502
- Demorest, P. B., Pennucci, T., Ransom, S., Roberts, M., & Hessels, J. 2010, *nature*, 467, 1081
- Dwyer, S., Sigg, D., Ballmer, S. W., et al. 2015, *Physical Review D*, 91, 082001
- Finn, L. S. 1992, *Physical Review D*, 46, 5236
- Finn, L. S., & Chernoff, D. F. 1993, *Physical Review D*, 47, 2198
- Fonseca, E., Pennucci, T. T., Ellis, J. A., et al. 2016, *The Astrophysical Journal*, 832, 167
- Forbes, M. M., Bose, S., Reddy, S., et al. 2019, *Physical Review D*, 100, 083010
- Frieman, J. A., Turner, M. S., & Huterer, D. 2008, *Annu. Rev. Astron. Astrophys.*, 46, 385
- Gupta, A., Fox, D., Sathyaprakash, B. S., & Schutz, B. F. 2019, *The Astrophysical Journal*, 886, 71
- Hinderer, T. 2008, *The Astrophysical Journal*, 677, 1216
- Hinderer, T., Lackey, B. D., Lang, R. N., & Read, J. S. 2010, *Physical Review D*, 81, 123016
- Iyer, B., Souradeep, T., Unnikrishnan, C., et al. 2011, *Ligo-india tech. rep.*(2011) URL <https://dcc.ligo.org/cgi-bin/DocDB/ShowDocument>
- Jaranowski, P., Krlak, A., & Schutz, B. F. 1998, *Physical Review D*, 58, 063001
- Kay, S. M. 1993, *Fundamentals of statistical signal processing, Volume I: Estimation Theory, Volume II: Detection Theory* (Pearson Education)
- Lackey, B. D., & Wade, L. 2015, *Physical Review D*, 91, 043002
- Landry, P. 2018, arXiv:1805.01882
- Li, L. X., & Paczyński, B. 1998, *The Astrophysical Journal*, 507, L59
- Lindblom, L. 1992, *The Astrophysical Journal*, 398, 569
- Linder, E. V. 2003, *Physical Review Letters*, 90, 091301
- Love, A. E. H. 1911, *Some problems in geodynamics* (Cambridge Univ. Press)
- Maggiore, M. 2008, *Gravitational Waves: Volume 1: Theory and Experiments* (New York: Oxford University Press)
- Markakis, C., Read, J. S., Shibata, M., et al. 2012, *The Twelfth Marcel Grossmann Meeting: On Recent Developments in Theoretical and Experimental General Relativity, Astrophysics and Relativistic Field Theories* (In 3 Volumes), 743
- Martinez, V. J., Saar, E., Gonzales, E. M., & Pons-Borderia, M. J. 2009, *Data Analysis in Cosmology*, Vol. 665 (Springer-Verlag Berlin Heidelberg)
- Messenger, C., & Read, J. 2012, *Physical review letters*, 108, 091101
- Miller, M., Lamb, F. K., Dittmann, A., et al. 2019, *The Astrophysical Journal Letters*, 887, L24
- Nakar, E. 2007, *Physics Reports*, 442, 166
- O’Shaughnessy, R. K. C. K. V., & Belczynski, K. 2008, *ApJ*, 672, 479
- Özel, F., & Freire, P. 2016, *Annual Review of Astronomy and Astrophysics*, 54, 401
- Punturo, M., Abernathy, M., Acernese, F., et al. 2010, *Classical and Quantum Gravity*, 27, 194002
- Raffai, P., Gondn, L., Heng, I. S., et al. 2013, *Classical and Quantum Gravity*, 30, 155004
- Read, J. S., Markakis, C., Shibata, M., et al. 2009, *Physical Review D*, 79, 124033
- Riley, T. E., Watts, A. L., Bogdanov, S., et al. 2019, *The Astrophysical Journal Letters*, 887, L21
- Sathyaprakash, B. S., & Schutz, B. F. 2009, *Living Reviews in Relativity*, 12, 2
- Sathyaprakash, B. S., Schutz, B. F., & Van Den Broeck, C. 2010, *Classical and Quantum Gravity*, 27, 215006
- Schutz, B. F. 1986, *Nature*, 323, 310
- Stairs, I. H. 2004, *Science*, 304, 547
- Tamanini, N., Caprini, C., Barausse, E., et al. 2016, *Journal of Cosmology and Astroparticle Physics*, 2016, 002
- Taylor, S. R., & Gair, J. R. 2012, *Physical Review D*, 86, 023502
- Thorsett, S. E., & Chakrabarty, D. 1999, *The Astrophysical Journal*, 512, 288
- Vines, J., Flanagan, E. E., & Hinderer, T. 2011, *Physical Review D*, 83, 084051
- Vines, J. E., & Flanagan, E. E. 2013, *Physical Review D*, 88, 024046
- Vitale, S., & Evans, M. 2017, *Physical Review D*, 95, 064052
- Vivanco, F. H., Smith, R., Thrane, E., et al. 2019, *Physical Review D*, 100, 103009
- Weber, F., Orsaria, M., Rodrigues, H., & Yang, S.-H. 2012, *Proceedings of the International Astronomical Union*, 8, 61
- Weinberg, S. 2008, *Cosmology* (Oxford University Press)
- Wen, L., & Chen, Y. 2010, *Physical Review D*, 81, 082001

- Xia, C., Zhu, Z., Zhou, X., & Li, A. 2019, arXiv:1906.00826
- Yan, C., Zhao, W., & Lu, Y. 2020, *The Astrophysical Journal*, 889, 79
- Yu, J., Wang, Y., Zhao, W., & Lu, Y. 2020a, arXiv:2003.06586
- Yu, J. M., Song, H., Ai, S., et al. 2020b, in preparation
- Zhang, X., Liu, T., & Zhao, W. 2017a, *Physical Review D*, 95, 104027
- Zhang, X., Yu, J., Liu, T., Zhao, W., & Wang, A. 2017b, *Physical Review D*, 95, 124008
- Zhao, W., & Santos, L. 2019, *Journal of Cosmology and Astroparticle Physics*, 2019, 009
- Zhao, W., Van Den Broeck, C., Baskaran, D., & Li, T. 2011, *Physical Review D*, 83, 023005
- Zhao, W., & Wen, L. 2018, *Physical Review D*, 97, 064031
- Zhou, E.-P., Zhou, X., & Li, A. 2018, *Physical Review D*, 97, 083015
- Zhu, Z.-Y., Zhou, E.-P., & Li, A. 2018, *The Astrophysical Journal*, 862, 98